

Accepted Manuscript

Magnetic and dipole moments in indium doped barium hexaferrites

S.V. Trukhanov, A.V. Trukhanov, V.A. Turchenko, An.V. Trukhanov, D.I. Tishkevich, E.L. Trukhanova, T.I. Zubar, D.V. Karpinsky, V.G. Kostishyn, L.V. Panina, D.A. Vinnik, S.A. Gudkova, E.A. Trofimov, P. Thakur, A. Thakur, Y. Yang

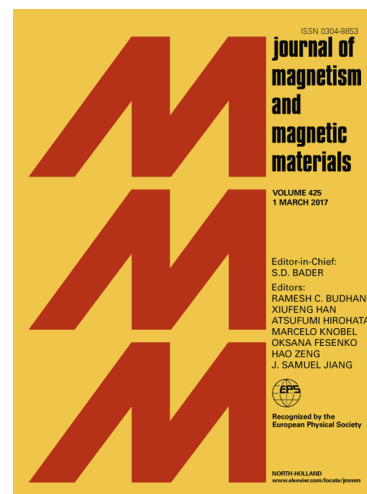
PII: S0304-8853(17)33841-6
DOI: <https://doi.org/10.1016/j.jmmm.2018.02.078>
Reference: MAGMA 63755

To appear in: *Journal of Magnetism and Magnetic Materials*

Received Date: 11 December 2017
Revised Date: 24 January 2018
Accepted Date: 23 February 2018

Please cite this article as: S.V. Trukhanov, A.V. Trukhanov, V.A. Turchenko, An.V. Trukhanov, D.I. Tishkevich, E.L. Trukhanova, T.I. Zubar, D.V. Karpinsky, V.G. Kostishyn, L.V. Panina, D.A. Vinnik, S.A. Gudkova, E.A. Trofimov, P. Thakur, A. Thakur, Y. Yang, Magnetic and dipole moments in indium doped barium hexaferrites, *Journal of Magnetism and Magnetic Materials* (2018), doi: <https://doi.org/10.1016/j.jmmm.2018.02.078>

This is a PDF file of an unedited manuscript that has been accepted for publication. As a service to our customers we are providing this early version of the manuscript. The manuscript will undergo copyediting, typesetting, and review of the resulting proof before it is published in its final form. Please note that during the production process errors may be discovered which could affect the content, and all legal disclaimers that apply to the journal pertain.



MAGNETIC AND DIPOLE MOMENTS IN INDIUM DOPED BARIUM HEXAFERRITES

S.V. Trukhanov^{1,2,3*}, A.V. Trukhanov^{1,2,3}, V.A. Turchenko^{4,5}, An.V. Trukhanov^{1,3}, D.I. Tishkevich²,
E.L. Trukhanova^{1,3}, T.I. Zubar⁶, D.V. Karpinsky³, V.G. Kostishyn¹, L.V. Panina¹, D.A. Vinnik²,
S.A. Gudkova^{2,7}, E.A. Trofimov², P. Thakur⁸, A. Thakur⁹, Y. Yang¹⁰

¹National University of Science and Technology MISiS, 119049, Moscow, Leninsky Prospekt, 4, Russia

²South Ural State University, 454080, Chelyabinsk, Lenin Prospect, 76, Russia

³SSPA “Scientific and practical materials research centre of NAS of Belarus”, 220072 Minsk, P. Brovki str., 19, Belorussia, * corresponding author e-mail: truhanov@ifttp.bas-net.by

⁴Joint Institute for Nuclear Research, 141980 Dubna, Joliot-Curie str., 6, Russia

⁵Donetsk Institute of Physics and Technology named after O.O. Galkin of the NAS of Ukraine, Prospect Nauky, 46, Kyiv, 03680, Ukraine

⁶A.V. Luikov Heat and Mass Transfer Institute of the NAS of Belarus, 220072 Minsk, P. Brovki str., 15, Belorussia

⁷Moscow Institute of Physics and Technology (State University), 141700, Institutskiy per. 9, Dolgoprudny, Russia

⁸Amity School of Applied Sciences, Amity University Gurgaon, Haryana, 122413 India

⁹Amity Centre of Nanotechnology, Amity University Gurgaon, Haryana, 122413, India

¹⁰Computational Physics Key Laboratory of Sichuan Province, School of Physics and Electronic Engineering, Yibin University, Yibin 644007, P. R. China

Crystal and magnetic structure of the doped $\text{BaFe}_{12-x}\text{In}_x\text{O}_{19}$ samples were refined by the results of investigations using high resolution neutron powder diffraction and vibration sample magnetometry at different temperatures. The refinements were realized in frame of two space groups. The $P6_3/mmc$ (No 194) centrosymmetric nonpolar and $P6_3mc$ (No 186) noncentrosymmetric polar space groups were used. The unit cell parameters, ionic coordinates, thermal isotropic factors, occupation positions, bond lengths and bond angles, microstrain values were established. The magnetic and dipole moments were also defined. It is established that the In^{3+} cations may be located only in the Fe1 - 2a and Fe2 - 2b crystallographic positions with equal probability for the sample with lowest substitution level $x = 0.1$. At the $x = 1.2$ substitution level about half of the In^{3+} cations occupies the Fe5 - 12k positions. For the last sample the remaining half of the In^{3+} cations is equiprobably located in the Fe1 - 2a and Fe2 - 2b positions. The spontaneous polarization was established for these compositions at 300 K. It is studied the influence of the type of substitutive cation and structural parameters on the $\text{Fe}^{3+}(i) - \text{O}^{2-} - \text{Fe}^{3+}(j)$ ($i, j = 1, 2, 3, 4, 5$) indirect superexchange interactions with temperature. With substitution level increase the superexchange interactions between the magnetic positions inside and outside the sublattices are broken which leads to a decrease in the value of their magnetic moments.

Keywords: substituted hexaferrites, neutron powder diffraction, crystal and magnetic structure, magnetic moment, spontaneous polarization.

1. INTRODUCTION

In last time, barium and strontium hexagonal ferrites continue to attract the close attention of researchers in various fields of science and technology [1-7]. These compounds were discovered in the early 50-ies of the last century [8]. Since then and until now, interest in these compounds has been increasing with increasing speed [9]. This behavior of researchers and engineers is not surprising, since it is explained by the huge presence of these materials in the modern industry. These compounds are the most common magnetic materials [10]. The main products of M-type hexaferrites are the magnetic credit cards, bar codes, rotors of small electromotors, as well as low-loss microwave devices.

At the moment, one of the interesting questions in the study of hexaferrites is the issue of origin of the appearance of spontaneous polarization at room temperature. Mechanism for its realization is also important [11-14]. This question presents both fundamental scientific interest and it is important from a practical point of view [15-25]. Some controversy about ferroelectricity in the M-type hexaferrites exists [26]. In [27] the large spontaneous polarization for these compounds has been revealed at 300 K. The most interesting is that the magnetoelectric characteristics of the M-type hexaferrites fabricated by a modified ceramic technique are more advanced [28] than those for the well-known room temperature BiFeO_3 multiferroic. The crystal structure of the barium hexaferrites in frame of $P6_3/mmc$ space group and the origin of the ferroelectricity were investigated by the lowering of crystal structure symmetry and by the distortion of FeO_6 oxygen octahedron [27].

The authors of [29] have studied the temperature dependence of the polar phonon modes in $\text{BaFe}_{12}\text{O}_{19}$ single crystal in the temperature range from 6 to 300 K and have concluded that the $\text{Fe}(2)$ cations move in a complex potential relief near the (2b) pentahedral positions with most likely three minima. At room temperature, the $\text{Fe}(2)$ cations exhibit rapid diffusion and dynamically occupy the (4e) positions. Below approximately 80 K this dynamic disorder gradually becomes a static and hexaferrite symmetry lowering to the polar phase with the space group $P6_3mc$.

In paper [30] it is reported that the M-type hexaferrites are a new family of magnetic quantum paraelectrics along the c-axis only, when the authors of [31] have theoretically predicted a paraelectric to antiferroelectric phase transition for the $\text{BaFe}_{12}\text{O}_{19}$ at about 3.0 K. They clearly demonstrated the lattice instability associated with the distribution of the Fe^{3+} cations over the (2b) pentahedral crystallographic positions. The ferroelectric state in barium hexaferrite, reachable by applying an external electric field to the antiferroelectric state, can be made stable at room temperature by appropriate element substitution or strain engineering. Thus the M-type hexaferrites are a new type of multiferroic with coexistence of antiferroelectricity and ferrimagnetism.

The diamagnetic substitution of the M-type hexaferrites can cause great interest [32-39] also because that the M-type hexaferrites exhibit a new mechanism for local electric dipoles formation based on the magnetic Fe^{3+} ($3d^5$) cation, violating the d^0 rule [40]. The competition between the long-range Coulomb interaction and short-range Pauli repulsion in a different oxygen coordination would favour an off-centre displacement of Fe^{3+} cation that induces a local electric dipole. In case of large concentration of d^5 cations in iron crystallographic positions so formed local dipoles cannot order down to the lowest temperatures. But the ferroelectric state at room temperature can be achieved using the local strains such as in thin films or the chemical substitutions such as in diamagnetically substituted solid solutions when the concentration of d^5

cations in iron crystallographic positions decreases. For the Al-substituted $\text{BaFe}_{12-x}\text{Al}_x\text{O}_{19}$ ($x \leq 1.2$) hexaferrites the existence of the spontaneous polarization $0.6 \mu\text{C}/\text{cm}^2$ in electric field of $110 \text{ kV}/\text{m}$ and the strong relationship 5 % of the dielectric and magnetic subsystems at room temperature were found [41]. Furthermore at the diamagnetic substitution the canted magnetic structure can occur, which also promotes the stabilization of the ferroelectric state [42]. The surface morphology of the crystallites and the magnetic properties of hexaferrites are highly dependent on small additions of B_2O_3 [43], Si_2O_3 [44] and CaO [45] oxides. While the crystal structure parameters almost do not change.

To this moment we have already completed a series of studies [46-50] of the crystal and magnetic structure by powder neutron diffractometry as well as the magnetic properties by vibration sample magnetometry for the $\text{BaFe}_{12-x}\text{Al}(\text{In})_x\text{O}_{19}$ ($x = 0.1-1.2$) solid solutions at room temperature. The atomic coordinates and lattice parameters have been Rietveld refined. In the present work we have carried out the thorough investigation of the effect of particular substitution of Fe^{3+} cations by diamagnetic In^{3+} cations on the crystal and magnetic structure and magnetic properties in a wide temperature range from 4 K up to 730 K for the $\text{BaFe}_{10.8}\text{In}_{1.2}\text{O}_{19}$ barium hexaferrite. The spontaneous polarization was established for these compositions at 300 K. The structure investigation was realized by high resolution neutron diffraction and the magnetic investigation was realized by vibration magnetometry. In the present work the temperature comparison of structure and magnetic parameters is given for the samples with two critical values of $x = 0.1$ and 1.2 .

2. EXPERIMENT

The investigated $\text{BaFe}_{11.9}\text{In}_{0.1}\text{O}_{19}$ and $\text{BaFe}_{10.8}\text{In}_{1.2}\text{O}_{19}$ polycrystalline samples have been obtained from high purity Fe_2O_3 (99.999%) and In_2O_3 (99.999%) oxides and carbonate BaCO_3 (chem. analysis purity) using conventional solid reaction method. The more detailed information about the samples preparation can be found in [50]. An X-ray analysis of the synthesized samples was carried out on a DRON-3 diffractometer with the K_α radiation of Cu at room temperature in the interval of angles $10^\circ \leq 2\Theta \leq 100^\circ$. A graphite monochromator was used to filter out the K_β -radiation. The content of oxygen was determined by a thermogravimetric analysis. The chemical composition and Fe/In ratio after synthesis have been estimated by Auger data (Scanning Auger Multiprobe PHI660, PerkinElmer) and X-ray activated analysis (Princeton Gamma-Tech, Inc.).

The powder neutron diffraction method with the time-of-flight (TOF) High Resolution Fourier Diffractometer (HRFD) at the IBR-2M pulsed reactor in Joint Institute for Nuclear Research, Dubna, Russia was used for the structure investigations at the 4 – 730 K [51]. The correlation technique of data acquisition is used, providing a very high resolution of $\Delta d/d \sim 0.001$, practically constant in a wide interval of d_{hkl} spacings. For the lattice parameters refinements the standard Al_2O_3 (standard SRM-676 of NIST, USA) was used. The low temperature ($< 300 \text{ K}$) was achieved using cool head model RDK-408 and the helium cryocooler of Sumitomo Heavy Industries Ltd. The high temperature was achieved with vanadium surface furnace and Eurotherm temperature controller. The refining of crystal and magnetic structures was performed by Rietveld analysis [52], using the FullProf [53] software program. Peak asymmetry correction was applied. Peak shapes were quantified by a pseudo-Voigt function. At the fitting the background intensities were refined using a Chebyshev polynomial function with six coefficients. Each structural model was refined to convergence with the best result selected on the basis of standard relevance factors and stability of the refinement. The more details about FullProf treatment may be found in [50].

The magnetic susceptibility and specific magnetization were measured at 4-730 K by Liquid Helium Free High Field Measurement System (VSM) [54]. The magnetic susceptibility was investigated in low magnetic field of 50 Oe. The specific magnetization was investigated in magnetic field of 10^4 Oe in heating and cooling mode. The ferrimagnet-paramagnet phase transition temperature - Curie temperature - has been defined as the inflection point in the temperature dependence of the specific magnetization [55].

The high-voltage dielectric polarization was measured at the 300 K temperature using the equipment, the details of which are described in [56]. The configuration of the electric field was used in the form of the sawtooth bipolar voltage pulses applied to the measured capacitor. The rise time of the sawtooth voltage was 0.1 s, and the frequency was 2.5 Hz. The pulses with a rise time of the sawtooth voltage of 0.05 s and 0.01 s, and a frequency of 5 Hz and 25 Hz were also used. The voltage amplitude was varied discretely from 200 V to 1000 V with a step of 200 V. The electrodes based on silver paste were used to perform the dielectric polarization measurements. The electric response was recorded with help of a high-impedance operational amplifier, the data from which were recorded via an ADC using a personal computer. The samples were short-circuited before the polarization measurement.

3. RESULTS AND DISCUSSION

3.1. Crystal structure

Results of NPD investigations and their treatment are shown in Fig. 1. In general case the NPD pattern consists from two contribution the crystal and magnetic. The crystal structure gives rise to the purely nuclear scattering part of the diffraction pattern. The magnetic structure gives rise to additional scattering which is superimposed on the nuclear scattering. This additional scattering depends on the magnetic moments to be associated with non-equivalent crystallographic positions, their orientation relative to each other and also on the magnetic form factors. To separate the magnetic and nuclear contributions to the diffraction peaks the samples were heated up above the T_c .

The Fig. 1 shows satisfactory agreement between the observed and calculated profiles. In this refining process the actual magnetic structure has been defined [57]. The $P6_3/mmc$ (No 194) space group was used at the analysis of the NPD data at $T = 730$ K, since it is a classical space group used to describe the crystal structure of M-type hexaferrites [58]. The unit cell has two formula units ($Z = 2$). The unit cell parameters, atomic coordinates, cation distribution and Rietveld relevance factors (R-factors) received during the processing of the NPD spectra in frame of this space group have been summarized in Table 1. The thermal vibrations of atoms were used in the isotropic approximation. The magnetic structure was used in the collinear approximation [58] at low temperatures. The low values of reliability factors suggest that the refinement of neutron data is effective.

The Fe^{3+} cation in the Fe1 – 2a position is 6-fold coordinated by the 6 O^{2-} anions in O4 positions (Fig. 2). The Fe^{3+} cation in the Fe2 – 2b position is 5-fold coordinated by the 2 O^{2-} anions in O1 polar positions and by the 3 O^{2-} anions in O3 equatorial positions. The Fe^{3+} cation in the Fe3 – $4f_{IV}$ position is 4-fold coordinated by the 1 O^{2-} anion in O2 polar position and by the 3 O^{2-} anions in O4 equatorial positions. The Fe^{3+} cation in the Fe4 – $4f_{VI}$ position is 6-fold coordinated by the 3 O^{2-} anions in O3 positions and by the 3 O^{2-} anions in O5 positions. The Fe^{3+} cation in the Fe5 – 12k position is 6-fold coordinated by the 1 O^{2-} anion in O3 position, by the 1 O^{2-} anion in O2 position, by the 2 O^{2-} anions in O4 positions and by the 2 O^{2-} anions in O5 positions [57].

Spontaneous polarization was previously observed in diamagnetic doped barium hexaferrites [13-21], but the mechanism of its appearance remains unclear. The appearance of a nonzero dipole electric moment, due to the distortion of the oxygen environment of the magnetoactive iron cations, can be a consequence of the order-disorder transition, which is undergoing crystal structure. As a result of appearance of a nonzero dipole electric moment the crystal structure of this solid solutions should be described in the framework of the noncentrosymmetric polar $P6_3mc$ (No. 186) space group at low temperatures. Therefore, the crystal structure of studied samples of indium doped barium hexferrites has been refined in frame of noncentrosymmetric polar $P6_3mc$ (No. 186) space group at 300 K and below.

NPD spectrum for $BaFe_{11.9}In_{0.1}O_{19}$ sample at 300 K refined in frame of $P6_3mc$ (No 186) space group is shown in Fig. 3. In the present paper, the refinement of the crystal structure was carried out for both possible variants for the $P6_3/mmc$ (No 194) centrosymmetric nonpolar and $P6_3mc$ (No 186) noncentrosymmetric polar space groups. The crystal structure parameters at 300 K room temperature in frame of this space group are given in Table 2. The refinement of unit cell parameters within the framework of the $P6_3/mmc$ (No 194) and $P6_3mc$ (No. 186) spatial groups showed their coincidence within the limits of statistical errors.

The temperature of ferroelectric ordering in M-type hexaferrites has not yet been determined exactly. However, taking into account the temperature dependence of the dielectric constant for $BaFe_{12-x}Cr_xO_{19}$ and the peak of this dependence in the region of 670 K [21], it can be assumed that T_C is below the magnetic ordering temperature for this class of compounds. Raman and infra-red spectroscopy of the high-temperature paraelectric and low-temperature ferroelectric phases showed only weak bands in the ferroelectric phase due to the non-centrosymmetry, indicating that the structural differences between the ferroelectric and paraelectric phases are very small [29]. Fe5 iron cation placed in the bipyramidal (2b) position plays a key role in the anisotropy of M-type hexaferrites. It is established that in addition to already existing ferrimagnetic order in $BaFe_{12}O_{19}$, a clear softening of the lowest A_{2u} polar mode suggests possible phase transition to the polar phase with $P6_3mc$ (No 186) space group and spontaneous polarization along the six-fold c -axis as a result of displacement of Fe5 cation from symmetry center [29]. The main symmetry differences between the two space groups $P6_3/mmc$ (No 194) and $P6_3mc$ (No 186) are that the oxygen coordination of the iron cations located in the octahedral $4f_{VI}$ and $12k$ symmetries is changing. To the Fe4 cation placed in $4f_{VI}$ position coordinated by the 3 O^{2-} anions in O3 positions and by the 3 O^{2-} anions in O5 positions and Fe5 cation placed in $12k$ position coordinated by the 1 O^{2-} anion in O3 position, by the 1 O^{2-} anion in O2 position, by the 2 O^{2-} anions in O4 positions and by the 2 O^{2-} anions in O5 positions in $P6_3/mmc$ (No 194) space group are added two new iron positions in $P6_3mc$ (No 186) space group Fe44 coordinated by the 3 O^{2-} anions in O3 positions and by the 3 O^{2-} anions in O55 positions and Fe55 coordinated by the 1 O^{2-} anion in O1 position, by the 1 O^{2-} anion in O22 position, by the 2 O^{2-} anions in O44 positions and by the 2 O^{2-} anions in O55 positions (see Table 2). For the Rietveld refinements in frame of $P6_3mc$ (No 186) space group at 300 K and below the reliability R-factors and χ^2 are lower than for the refinements in frame of $P6_3/mmc$ (No 194) space group which indicates the truth of our assumption.

The coherent scattering lengths for the Fe^{3+} and In^{3+} cations differ significantly $f_{Fe} = 9.450$ barn and $f_{In} = 4.065$ barn. This is good condition for the fitting of the occupation value of the different crystallographic positions. The determination of the occupancy positions added some difficulties when the NPD are analyzed since the number of variable parameters increases. Structural refinement for the $BaFe_{10.8}In_{1.2}O_{19}$ sample in frame of both space group

shows that about half of the In^{3+} cations (47%) occupy the octahedral Fe5 – 12k positions. The remaining In^{3+} cations are distributed almost evenly among the octahedral Fe1 – 2a and bipyramidal Fe2 – 2b positions. The larger multiplicity of the 12k position gives a small content ratio of $\sim 4\%$ for In^{3+} cations on the Fe5 – 12k position. It is found no occupancy at the Fe3 – 4f_{IV} and Fe4 – 4f_{VI} positions, and the In^{3+} cations prefer the Fe1 – 2a, Fe2 – 2b and Fe5 – 12k positions. All the possible and the most likely combinations of the occupation of all the nonequivalent crystallographic positions by the In^{3+} cations were consistently tried. The optimum values of the R-factors were established. After this combinatorial analysis the most likely distribution of the In^{3+} cations with temperature change was found. The errors of the positions occupancy refinements were sufficiently small ($< 10^{-6}$). The preference positions are also in agreement with the changes in bond distances from pure $\text{BaFe}_{12}\text{O}_{19}$ and lightly In-substituted $\text{BaFe}_{11.9}\text{In}_{0.1}\text{O}_{19}$ sample which we will see below.

For the $\text{BaFe}_{11.9}\text{In}_{0.1}\text{O}_{19}$ sample the In^{3+} cations have equal probability for location only in the Fe1 - 2a and Fe2 - 2b positions [59]. In this case the discrepancy between the experimental data and the performed calculations of the crystal and magnetic structures is minimal. It is interesting that the In-occupation behavior at large $x = 1.2$ substitution level is similar to the Al-occupation behavior at small substitution level $x = 0.1$ in a wide temperature range [59].

The unit cell parameters for the $\text{BaFe}_{10.8}\text{In}_{1.2}\text{O}_{19}$ sample are shown in F. 4. At 300 K they are $a = 5.9326(2)\text{ \AA}$, $c = 23.4458(9)\text{ \AA}$, $V = 714.64(5)\text{ \AA}^3$ (see Fig. 4 and Table 1). It is well known that for the parent un-substituted $\text{BaFe}_{12}\text{O}_{19}$ hexaferrite at 300 K the unit cell parameters are $a = 5.893\text{ \AA}$, $c = 23.194\text{ \AA}$, $V = 697.5\text{ \AA}^3$ [60]. These parameters are obtained by the powder X-ray diffraction method and their accuracy may not very high. The addition to the parent $\text{BaFe}_{12}\text{O}_{19}$ compound of the In^{3+} cations with $x = 0.1$ and 1.2 concentration retains single phase sample. This is fixed by the absence of the new nuclear diffraction reflections on NPD spectrum. The solid solutions on base of barium hexaferrite form with $a = 5.8955(2)\text{ \AA}$, $c = 23.2173(7)\text{ \AA}$, $V = 698.84(3)\text{ \AA}^3$ [57] and $a = 5.9326\text{ \AA}$, $c = 23.4458\text{ \AA}$, $V = 714.64\text{ \AA}^3$ [50] unit cell parameters at 300 K for the $x = 0.1$ and 1.2 , respectively. The unit cell parameters for the $x = 0.1$ are larger than the unit cell parameters for the parent compound and smaller than the unit cell parameters for the $x = 1.2$. It is due to the larger ionic radii of the In^{3+} cation (0.940 \AA) unlike of the Fe^{3+} (0.690 \AA) cation [61].

With the temperature increase up to 730 K all the unit cell parameters rise too. However, this parameters rise is not linear (Fig. 4). At 300 K the smallest differences between unit cell parameters for the $x = 0.1$ and $x = 1.2$ are revealed. So, a parameter for the $x = 1.2$ at 300 K is larger than a parameter for the $x = 0.1$ on 0.63% . At 10 K and 730 K this value is 0.76% and 0.83% , respectively. The c parameter for the $x = 1.2$ at 300 K is larger than c parameter for the $x = 0.1$ on 0.98% . At 10 K and 730 K this value is 1.29% and 1.04% , respectively. For the V unit cell volume at 10 K, 300 K and 730 K this value is 2.85% , 2.26% and 2.73% , respectively.

Some comparison of effect of the Al^{3+} and In^{3+} cations on the structural parameters of the barium hexaferrite may be made. For the $\text{BaFe}_{11.9}\text{Al}_{0.1}\text{O}_{19}$ hexaferrite at 300 K the unit cell parameters are $a = 5.8898(2)\text{ \AA}$, $c = 23.1971(6)\text{ \AA}$, $V = 696.91(3)\text{ \AA}^3$ [59]. They are smaller than the unit cell parameters for the parent $\text{BaFe}_{12}\text{O}_{19}$ and the $\text{BaFe}_{11.9}\text{In}_{0.1}\text{O}_{19}$ hexaferrites. It is due to the larger ionic radii of the In^{3+} cation (0.940 \AA) and the smaller ionic radii of the Al^{3+} cation (0.535 \AA) unlike of the Fe^{3+} (0.690 \AA) cation [61]. At the fixed 300 K temperature the V unit cell volume for the Al-substituted samples is changed with rate of $dV/dx = -10.04\text{ \AA}^3$ [46], while for the In-substituted samples it is changed with rate of $dV/dx = 14.82\text{ \AA}^3$ [49]. The negative changing rate of the V unit cell volume for the Al-substituted samples indicates on the decrease

of the lattice parameters with substitution. While the temperature increases the parameters and the volume of the unit cell are increased for all the samples as for the Al-substituted and the In-substituted ones remaining larger in the last case for the larger substitution level (Fig. 4).

While the temperature decreases the lattice parameters are decreased. It is due to the decreasing of the thermal energy of the random motion of ions. The coefficients of linear and volume thermal expansion are calculated as in [50]. The high anisotropy of crystal structure leads to difference of the coefficient of linear thermal expansion for a ($\alpha_a \sim 7.51 \cdot 10^{-6} \text{ K}^{-1}$ ($x = 0.1$) and $\alpha_a \sim 7.42 \cdot 10^{-6} \text{ K}^{-1}$ ($x = 1.2$)) and c ($\alpha_c \sim 13.11 \cdot 10^{-6} \text{ K}^{-1}$ ($x = 0.1$) and $\alpha_c \sim 12.89 \cdot 10^{-6} \text{ K}^{-1}$ ($x = 1.2$)) axis. The coefficient of volume thermal expansion is $\alpha_v \sim 27.82 \cdot 10^{-6} \text{ K}^{-1}$ ($x = 0.1$) and $\alpha_v \sim 27.65 \cdot 10^{-6} \text{ K}^{-1}$ ($x = 1.2$).

At low ($< 150 \text{ K}$) temperatures the Invar effect, i.e. quasi-zero thermal expansion coefficient, is observed both for the samples (Fig. 4). In this range the temperature decreasing leads to low increase of the unit cell a and c parameters and V volume. Similar dependence of the unit cell parameters at low temperatures was observed earlier in the metallic oxides [62]. The most likely explanation of the Invar effect is the anharmonicity of low energy phonon modes.

The temperature dependences of the main Fe-O bond lengths and Fe-O-Fe bond angles for the $\text{BaFe}_{12-x}\text{In}_x\text{O}_{19}$ $x = 0.1$ and 1.2 refined from NPD are shown in Figs. 5, 6. Any abrupt changes of the structural parameters from 4 K up to 730 K were not found. For the $x = 0.1$ the majority of the bond lengths decrease with temperature decreasing. The Fe1-O4, Fe2-O3 and Fe3-O2 bond lengths increase with temperature decreasing. The most changes in the bond lengths are detected for the Fe2 cation relative to the O3 anion, for the Fe4 cation relative to the O5 anion and for the Fe4 cation relative to the O3 anion (Fig. 5a, b, c). With the concentration level increase up to $x = 1.2$ almost all the bond lengths change the behavior with temperature. Only the Fe5-O1 bond length continues to decrease when temperature decrease (Fig. 5c). In this case the most changes in the bond lengths are detected for the Fe5 cation relative to the O2 anion, for the Fe5 cation relative to the O1 anion and for the Fe2 cation relative to the O3 anion. The some bond lengths for the $x = 1.2$ become more (Fe2-O3 and Fe4-O5) or less (Fe3-O4 and Fe4-O3) the corresponding bond lengths for the $x = 0.1$ with temperature increase.

For the $x = 0.1$ the Fe2-O3-Fe4, Fe5-O1-Fe5 and Fe5-O4-Fe5 bond angles decrease with temperature decreasing while the Fe3-O4-Fe5, Fe5-O2-Fe5 and Fe4-O3-Fe4 bond angles increase (Fig. 6). The most changes in the bond angles are detected for the Fe4-O3-Fe4, Fe5-O2-Fe5 (they increase) and Fe5-O4-Fe5 (it decreases) as temperature decreases. The behavior changing similar to bond lengths is shown for the temperature dependences of the main bond angles with the concentration level increase (Fig. 6). With indium concentration increase from $x = 0.1$ up to $x = 1.2$ the Fe2-O3-Fe4, Fe5-O2-Fe5 and Fe4-O3-Fe4 bond angles change the correlation. It can be concluded that the Fe^{3+} (In^{3+}) cations in the octahedral 2a and 12k and pentahedral 2b positions are experienced the largest displacement with temperature and substitution level changing. And with the x increase the temperature behavior of the bond characteristics is reversed.

3.2 Polarization, magnetic and dipole moments

In the $\text{BaFe}_{12}\text{O}_{19}$ compound all the iron cations have $3+$ valency based on the law of the electroneutrality of macrobodies. The indium doping is the isovalent doping, i.e. indium cations have $3+$ valency. Thus all the iron cations are Fe^{3+} ones in the $\text{BaFe}_{12}\text{O}_{19}$ compound and $\text{BaFe}_{12-x}\text{In}_x\text{O}_{19}$ solid solutions with $x = 0.1$ and 1.2 .

Fig. 7 shows the hysteresis loops of the dielectric polarization at room temperature for the $\text{BaFe}_{12-x}\text{In}_x\text{O}_{19}$ samples with $x = 0.1$ and 1.2 . The maximum value of the electric field, which

could be achieved without the occurrence of the electric breakdown, was 97 kV/m. In this electric field, the spontaneous polarization for the $x = 1.2$ sample was 4.0 mC/m^2 . This value of the spontaneous polarization is approximately 2 orders of magnitude lower than the value obtained in [27, 28] and 3 orders of magnitude more than in [42]. The reason for this result was the significant leakage currents that occur because of the low resistivity of the samples. In work [28], the maximum electric fields were approximately three times larger. Since the magnitude of the resistivity plays a significant role at the recording of the polarization in the magnetic materials, then by the significant improvement of the preparation technology of the samples the significant increase of the polarization can be achieved in the future [28]. In the electric field of the 93 kV/m, the spontaneous polarization for the $x = 0.1$ sample was 3.7 mC/m^2 . With the increase of the x substitution level from 0.1 up to 1.2, the value of spontaneous polarization increased by approximately 10 %.

The main problem in the investigation of the polarization is the strong influence of the electric conductivity of the materials under study. The presence in the samples of the finite conductivity, which can depend strongly on the temperature and frequency and also on the amplitude of the applied voltage, gives its definite contribution to the measured polarization. To obtain a correct picture of the true polarization processes, this contribution of the conductivity must be separated from the polarization associated with the displacement of the ions. So, at the 300 K, the conductance of the samples under study was of the order of $10^{-9} \Omega \cdot \text{cm}$ and was independent of the temperature, as well as the frequency and amplitude of the alternating voltage in the used range. The reactance should increase with increasing of the frequency of the alternating voltage. This can lead to a decrease in the polarization. The reactance should not depend on the amplitude of the frequency of the alternating voltage. In our case, with the increase in the frequency from 2.5 Hz up to 25 Hz, the decrease of the maximum polarization by 10 % was experimentally observed. This behavior of the polarization indicates that the main contribution to its formation is given by the processes associated with the displacement of the ions.

With the substitution level increase the spontaneous polarization slightly increases up to 10 %. This is due to the increase of the concentration of the empty d-shells and the formation of the strong asymmetric covalent bonds in the Fe5 - 12k crystallographic position. In addition, since the In^{3+} cation has the ionic radius larger than the Fe^{3+} cation, the increase of the substitution concentration causes the local distortions and microstrains of the crystal lattice. This also contributes to the increase of the spontaneous polarization. It is still too early to say the anything about the permittivity and the loss tangent, as well as about their concentration, temperature and frequency dependence. But as it follows from [63], with the substitution level increase by the aluminum cations from $x = 0.5$ up to $x = 3.5$ at room temperature, the dielectric constant and the loss tangent decrease for the same frequency of the alternating current.

Comparison of the structural features of two spatial groups the centrosymmetric nonpolar $P6_3/mmc$ (No. 194) and the noncentrosymmetric polar $P6_3mc$ (No. 186) makes it possible to understand the cause of the occurrence of a nonzero dipole electric moment. In four oxygen octahedra the distances between the iron cations located at positions $4f_{VI}$ ($P6_3/mmc$) and oxygen anions (Fig. 8) are 2.148 \AA and 1.965 \AA for Fe4 - O3 and Fe4 - O5, respectively, at different substitution levels of In cations (Table 3). However, due to the presence of an inversion center in $P6_3/mmc$ space group, such displacements of iron cations with respect to the local centers of symmetry of the oxygen octahedra, compensate each other and do not lead to the appearance of a nonzero dipole electric moment.

When considering similar four oxygen octahedra in the case of $P6_3/mc$ (No. 186) space group the different degrees of their distortion are observed. For example, for the composition $x = 0.1$: in two octahedra (Table 4) the inter-ion distances of Fe4 - O3 and Fe4 - O5 have the values of 2.215 Å and 1.879 Å, respectively, and in the other two octahedra (Fig. 8a and b) the distances of Fe44 - O3 and Fe44 - O55 have the values of 1.961 Å and 2.079 Å, respectively. Such a difference in the distortion of oxygen octahedra in $P6_3/mc$ space group due to the absence of an inversion center may be the reason for the appearance of a nonzero dipole electric moment, which leads to the appearance of spontaneous electric polarization in solid solutions of barium hexaferrites.

A similar displacement of iron ions is observed in twelve oxygen octahedra at positions 12k ($P6_3/mmc$) (Table 4). Distances between Fe5-O4 and Fe5-O5 ions for sample $x = 0.1$ have the values of 2.104 Å and 1.928 Å, respectively. The values of the interatomic distances within the oxygen environment with an increase in the concentration of indium diamagnetic ions are given in Table 3.

Accordingly, for $P6_3/mc$ space group from twelve oxygen octahedral, located in crystallographic positions similar to $P6_3/mmc$ space group, the six octahedra at position 6c (Fig. 8c), have different displacement of iron cations from the local center of symmetry, compared to six others (Fig. 8d).

The temperature dependence of the specific magnetization and inverse magnetic susceptibility for the $BaFe_{12-x}In_xO_{19}$ $x = 0.1$ and 1.2 is given in Fig. 9. The T_C for the $BaFe_{11.9}In_{0.1}O_{19}$ is 692 K and for the $BaFe_{10.8}In_{1.2}O_{19}$ T_C is 550 K, whereas for the un-doped $BaFe_{12}O_{19}$ the T_C is 740 K [64]. Such magnetic parameters as the T_C Curie temperature and M_S spontaneous magnetization are determined by the intensity of the $Fe^{3+}(i) - O^{2-} - Fe^{3+}(j)$ ($i, j = 1, 2, 3, 4, 5$) indirect superexchange interactions. The intensity of these indirect superexchange interactions is determined, in turn, by the periodicity of the exchange-linked chains and such structural parameters as the bond length and bond angle. These indirect superexchange interactions have different sign, i.e. they are competing. T_C can also be expressed in terms of the number of $Fe^{3+}(i) - O^{2-} - Fe^{3+}(j)$ indirect superexchange interactions. This is in agreement with a similar explanation provided by [65].

The presence of the diamagnetic In^{3+} cations in the solid solutions leads to reduce of the number of neighbors of magnetic Fe^{3+} cations and so that the magnetic order is destroyed at lower temperatures [66]. At 4 K in 1 T the specific magnetization is 67 emu/g for the $BaFe_{11.9}In_{0.1}O_{19}$ and 58 emu/g for the $BaFe_{10.8}In_{1.2}O_{19}$. This is lower than for the un-doped sample. The reduction of the magnetization was caused by the incomplete coordination of the Fe^{3+} cations on the particle surface leading to a noncollinear spin configuration, which causes the formation of a surface spin canting.

The specific magnetization continuously decreases from 4 K up to 730 K. This peculiar shape of the $M(T)$ curves in hexaferrites is due to the temperature dependence of the magnetic moments of iron cations in the Fe5 - 12k positions. Such temperature variations of the hyperfine fields of the Fe5 - 12k positions and the subsequent decrease of curvature of $M(T)$ with x increase have already been demonstrated for the substituted $Sr_{1-x}La_xFe_{12-x}Co_xO_{19}$ ferrites [67]. This broad transition to the paramagnetic state resembles a second-order phase transition. The absence of the temperature hysteresis of the specific magnetization is also characteristic of the second-order phase transition. The continuous decrease of the specific magnetization may be understood in term of destroy of the intersublattice $Fe^{3+}(i) - O^{2-} - Fe^{3+}(j)$ ($i \neq j$) exchange interactions and the intrasublattice $Fe^{3+}(i) - O^{2-} - Fe^{3+}(j)$ ($i = j$) indirect superexchange interactions.

The inverse magnetic susceptibility is given on Fig. 9b. For both samples only positive value of the Θ_p paramagnetic Curie temperature is observed. For the $x = 0.1$ the Θ_p is 689 K whereas for the $x = 1.2$ it is 547 K. This is slightly less than T_C . This fact indicates on the dominant character of the ferromagnetic intrasublattice $\text{Fe}^{3+}(i) - \text{O}^{2-} - \text{Fe}^{3+}(j)$ ($i = j$) indirect superexchange interactions. High temperature susceptibility for both samples obeys the Curie-Weiss law. The Curie constant is $C \sim \text{ctg}\alpha$ proportional to the slope of the tangent to the inverse susceptibility and depends on the In^{3+} cations concentration. For the $x = 0.1$ the C is slightly less than for the $x = 1.2$. The $\mu_{\text{eff}} \sim C^{1/2}$ effective magnetic moment in paramagnetic region (> 740 K) behaves similar to the C [68]. This fact indicates the decrease of average magnetic moment per one Fe^{3+} cation with substitution as the trend. With x increase the positive $\text{Fe}^{3+}(i) - \text{O}^{2-} - \text{Fe}^{3+}(j)$ ($i = j$) interactions in particular magnetic sublattice are broken by introduction of the diamagnetic In^{3+} cations.

From [69] it is well known that for the complex 3d-metall oxide compounds the I intensity of the intrasublattice indirect superexchange interactions depends on both the $\text{M}^{\text{v}+} - \text{O}^{2-} - \text{M}^{\text{v}+}$ bond angles and $\text{M}^{\text{v}+} - \text{O}^{2-}$ bond lengths through the overlap integrals between the 3d-orbitals of the M metal cation and the 2p-orbitals of the O^{2-} anion. This I intensity is $I \sim \cos(\text{M}^{\text{v}+} - \text{O}^{2-} - \text{M}^{\text{v}+})$ directly proportional to cosine of the bond angle and $I \sim 1/(\text{M}^{\text{v}+} - \text{O}^{2-})$ inversely proportional to bond length. Based on this modeling approach and Figs. 4, 5 it can be concluded that the main contribution to the weakening of the magnetic ordering at low temperatures follows from the destruction of the intersublattice $\text{Fe}^{3+}(i) - \text{O}^{2-} - \text{Fe}^{3+}(j)$ ($i \neq j$; $i, j = 3, 4, 5$) exchange interactions between Fe3, Fe4, Fe5 sublattices. The Fe^{3+} and In^{3+} cations in the Fe4 - $4f_{\text{IV}}$ and Fe5 - 12k positions are responsible for the spontaneous polarization origin.

The maximum specific magnetization value decreases with temperature increasing. The atomic magnetic moment for both the samples is not saturated in external magnetic fields up to 2 T at all temperatures below T_c [70]. The consolidated ordered magnetic moment at 10 K in field of 2 T is $16 \mu_{\text{B}}$ per formula unit or $1.3 \mu_{\text{B}}$ per nominal Fe^{3+} cation for the $\text{BaFe}_{11.9}\text{In}_{0.1}\text{O}_{19}$ sample and $13 \mu_{\text{B}}$ per formula unit or $1.1 \mu_{\text{B}}$ per nominal Fe^{3+} cation for the $\text{BaFe}_{10.8}\text{In}_{1.2}\text{O}_{19}$ sample. Taking into account the magnetic structure of M-type hexaferrite according to Gorter's model [58] with iron up-spins on Fe1 - 2a, Fe2 - 2b and Fe5 - 12k positions and down-spins on Fe3 - $4f_{\text{IV}}$ and Fe4 - $4f_{\text{VI}}$ positions, a moment per formula unit of $20 \mu_{\text{B}}$ is expected for the $\text{BaFe}_{12}\text{O}_{19}$ in perfect collinear case in ground state. Assuming the In^{3+} cations to be located at up-spin Fe1 - 2a, Fe2 - 2b and Fe5 - 12K positions the consolidated ordered magnetic moment of $19.5 \mu_{\text{B}}$ per formula unit is expected for the $\text{BaFe}_{11.9}\text{In}_{0.1}\text{O}_{19}$ and $14 \mu_{\text{B}}$ per formula unit for the $\text{BaFe}_{10.8}\text{In}_{1.2}\text{O}_{19}$. The measured maximum magnetic moment is some smaller compared to calculated one. Some reduction of the consolidated moment might be caused by the incomplete coordination of the Fe^{3+} cations on the particle surface leading to a noncollinear spin configuration, which causes the formation of a surface spin canting [71].

As a result of partial substitution of the Fe^{3+} cations by the diamagnetic In^{3+} cations which are distributed statistically equivalent for the Fe1 - 2a, Fe2 - 2b and Fe5 - 12k positions it can be expected to change in the values of the magnetic moments in corresponding positions. Fig. 10 shows the values of the comparative temperature dependence of the magnetic moments of Fe^{3+} cations in the different crystallographic positions : Fe1 - 2a, Fe2 - 2b, Fe3 - $4f_{\text{IV}}$, Fe4 - $4f_{\text{VI}}$ and Fe5 - 12k for the $x = 0.1$ and 1.2.

The absence of the additional magnetic peaks determines the wave vector of the ferromagnetic structure as $\mathbf{k} = [0, 0, 0]$. The magnetic structure in all the temperature range fully satisfies the model proposed by Gorter [58]. All the magnetic moments of the Fe^{3+} cations are

oriented along the easy direction coinciding with the hexagonal c axis. The entering of the canting angle in each crystallographic position or in all positions together at the refinement procedure did not lead to decrease of the R-factors.

Earlier the J exchange integrals for the parent $\text{BaFe}_{12}\text{O}_{19}$ were calculated using the generalized gradient approximation considering the U Hubbard parameter method [72]. Taking into account different values of exchange integrals based on different experimental crystal structure parameters the dominant antiferromagnetic nature of the $\text{Fe}^{3+}(\text{i}) - \text{O}^{2-} - \text{Fe}^{3+}(\text{j})$ ($\text{i}, \text{j} = 1, 2, 3, 4, 5$) indirect superexchange interactions was revealed. The exchange integrals within the block layers were estimated to be order of 10^{-3} eV for the superexchange interactions such as Fe1 - Fe3 and Fe2 - Fe4. The large exchange integrals have large bond angles of 125.119° for the Fe1 - O4 - Fe3 and 138.421° for Fe2 - O3 - Fe4 [73]. The strength of the superexchange interaction follows the Goodenough–Kanamori rules increasing as the $\text{Fe}^{3+} - \text{O}^{2-} - \text{Fe}^{3+}$ bond angle deviates from 180° [74].

It can be assumed that at a low concentration of the In^{3+} cations in the solid solution they should be distributed statistically throughout nonequivalent crystallographic positions of the hexaferrite. However in our case to reduce the discrepancy between the experimental data and performed calculations of the magnetic and crystal structure it is established that the In^{3+} cations in a greater degree were preferred to the substitution of Fe^{3+} cations into the Fe1 - 2a and Fe2 - 2b crystallographic positions for small $x = 0.1$ level, while for the large $x = 1.2$ level they were preferred to the substitution into the Fe1 - 2a, Fe2 - 2b and Fe5 - 12k crystallographic positions.

We analyzed the temperature behavior of magnetic moment in each crystallographic position taking into account the In^{3+} cation distribution. The every magnetic moment of $x = 1.2$ is always larger than every magnetic moment of $x = 0.1$ (see Fig. 10). The corresponding magnetic moments are close and large in the Fe1 - 2a and Fe2 - 2b positions practically at all the temperatures. They are close and small in the Fe3 - $4f_{\text{IV}}$ and Fe4 - $4f_{\text{VI}}$ positions. This feature is shown both for the $x = 0.1$ and $x = 1.2$. There are considerable differences for the total magnetic moment and magnetic moment in Fe5 - 12k position for both the samples. This is explained by the In^{3+} cation distribution with substitution concentration increase. For some types of magnetic moment the nonmonotonic changing with temperature increase is observed. For the small $x = 0.1$ substitution concentration the magnetic moment in the Fe3 - $4f_{\text{IV}}$ and Fe4 - $4f_{\text{VI}}$ positions has inflection point in the 100 - 150 K temperature range. With concentration increase up to $x = 1.2$ the inflection point appears for the Fe1 - 2a and Fe2 - 2b crystallographic positions. The presence of the inflection point can be explained by the temperature behavior of the bond lengths and bond angles with substitution concentration increase. Below the 300 K the magnetic moments in the Fe1 - 2a and Fe2 - 2b positions are equal for both the $x = 0.1$ and $x = 1.2$. At low 10 K temperature the largest $\sim 32\%$ difference in magnetic moments of the $x = 0.1$ and $x = 1.2$ is observed for the Fe5 - 12k position. The smallest $\sim 8\%$ difference is observed for the Fe3 - $4f_{\text{IV}}$ and Fe4 - $4f_{\text{VI}}$ positions.

If the magnetic moment of Fe^{3+} cation at 0 K is equal $5 \mu_{\text{B}}$ then total magnetic moment of parent $\text{BaFe}_{12}\text{O}_{19}$ will be equal to $20 \mu_{\text{B}}$ per formula unit in case of perfect collinear magnetic structure. Such low $18.2 \mu_{\text{B}}$ for the $x = 0.1$ and $13.4 \mu_{\text{B}}$ for the $x = 1.2$ value of total magnetic moment obtained in present investigation is explained by influence of the diamagnetic In^{3+} cations and thermal factor causing the disorientation of the magnetic moments in space due to the increase of the thermal fluctuations.

In Fig. 11 the illustration of the spontaneous polarization origin in the $\text{BaFe}_{12-x}\text{In}_x\text{O}_{19}$ samples as a consequence of the distortion of the oxygen octahedron in the crystallographic Fe4 - $4f_{\text{VI}}$

and Fe5 - 12k positions is presented. It is well known that the crystal structure of M-type hexaferrites is stacked in the alternating order of the RSR*S* blocks along the *c* axis. S and S* are spinel blocks, R and R* are hexagonal barium-containing blocks. The S(R) and S*(R*) blocks are mirror-symmetrical with respect to the *ab* plane along the *c* axis. For the Fe5 - 12k position the noncentrosymmetric displacement of the Fe³⁺(In³⁺) cation to one from the O1 and O2 apical anions is only possible. As it can be seen from the Fig. 5 the Fe³⁺(In³⁺) cation is shifted to the O2 anion with temperature increase. The Fe5 – O1 bond length increases and the Fe5 – O2 bond length decreases when temperature increases from 4 K up to 730 K. This behavior is most pronounced for the composition with *x* = 1.2. For the *x* = 0.1 the tendency of the Fe5 – O2 bond length decreasing is less noticeable. This correlates with the distribution of the indium cations between the crystallographic positions when the substitution level increases. The displacement of the Fe³⁺(In³⁺) cation to the O2 anion in the S and S* leads to the appearance of the nonzero dipole moment. As a consequence of this displacement of the Fe³⁺(In³⁺) cation in Fe5 – 12k position to the O2 anion and the appearance of the nonzero dipole moment the *z*-component of the spontaneous polarization is formed. The spontaneous polarization increasing up to 10 % with the substitution level increase is explained by the increasing of the concentration of the empty *d*-shells and the formation of the strong asymmetric covalent bonds in the Fe5 - 12k crystallographic position. In addition, since the In³⁺ cation has the ionic radius larger than the Fe³⁺ cation, the increase of the substitution concentration causes also the local distortions and microstrains of the crystal lattice.

Conclusions

The diamagnetic substituted BaFe_{12-x}In_xO₁₉ solid solutions with *x* = 0.1 and *x* = 1.2 are synthesized by usual ceramic technology. These samples are investigated by high resolution neutron powder diffraction and vibration sample magnetometry in a wide temperature range of 4 – 730 K. The analysis of NPD data was performed by Rietveld method using the FullProf software program. The refinements were realized in frame of two space groups. The P6₃/mmc (No 194) centrosymmetric nonpolar and P6₃mc (No 186) noncentrosymmetric polar space groups were used. The temperature dependence of the crystal and magnetic structure features and exchange interactions are studied. It is established the unit cell parameters, ionic coordinates, thermal isotropic factors, positions occupation, bond lengths and bond angles, magnetic parameters and magnetic moments. The spontaneous polarization was established for these compositions at 300 K. It is studied the influence of structural parameters on the Fe³⁺(*i*) - O²⁻ - Fe³⁺(*j*) (*i*, *j* = 1, 2, 3, 4, 5) indirect superexchange interactions with temperature. The comparative analysis of the structural features and exchange interactions is carried out for the samples with two critical *x* = 0.1 and 1.2 values of concentration. As a consequence of the displacement of the Fe³⁺(In³⁺) cations in crystallographic Fe4 – 4f_{VI} and Fe5 – 12k positions to the O5 and O55 anions and the appearance of the nonzero dipole electric moment the *z*-component of the spontaneous polarization is formed.

Acknowledgement

This work was carried out with a financial support in part from the Ministry of Education and Science of the Russian Federation in the framework of Increase Competitiveness Program of NUST «MISiS» among the leading world scientific and educational centers (No. P02-2017-2-4, No. K4-2017-041, No. K3-2017-059), by the Belarusian Republican Foundation for Basic Research (No. F17D-003, No F18R-088) and Joint Institute for Nuclear Research (No. 04-4-1121-2015/2017). This work was partially supported by the Ministry of Education and Science of the Russian Federation (Government task in SUSU 5.5523.2017/8.9 and the framework of

Increase Competitiveness Program of MISiS G02-2017-2-4). Additionally this work was performed using equipment of MIPT Shared Facilities Center and with financial support from the Ministry of Education and Science of the Russian Federation (Grant No. RFMEFI59417X0014). Yujie Yang is thankful to the Scientific Research Fund of SiChuan Provincial Education Department for its funding through the Project No. 16ZA0330, and the Major Project of Yibin City of China for its funding through the Project No. 2016GY025. L. Panina acknowledges support under the Russian Federation State contract for organizing a scientific work. The authors express special gratitude to Professor A.M. Balagurov for his help and support.

REFERENCES

1. N. Yasmin, M. Mirza, S. Muhammad, M. Zahid, M. Ahmad, M.S.Awan, A. Muhammad, J. Magn. Mater. 446 (2018) 276-281.
2. S.J. Feng, J.L. Ni, X.H. Zhou, X.S. Wu, S.G. Huang, X.S. Liu, J. Magn. Mater. 447 (2018) 21-25.
3. K.M.U. Rehman, X. Liu, Y. Yang, S. Feng, J. Tang, Z. Ali, Z. Wazir, M.W. Khan, M. Shezad, M.S. Iqbal, C. Zhang, C. Liu, J. Magn. Mater. 449 (2018) 360-365.
4. J.-L. Mattei, C.N. Le, A. Chevalier, A. Maalouf, N. Noutehou, P. Queffelec, V. Laur, J. Magn. Mater. 451 (2018) 208-213.
5. S. Asiri, S. Güner, A.D. Korkmaz, Md. Amir, K.M. Batoo, M.A. Almessiere, H. Gungunes, H. Sözeri, A. Baykal, J. Magn. Mater. 451 (2018) 463-472.
6. H. Feng, D. Bai, L. Tan, N. Chen, Y. Wang, J. Magn. Mater. 433 (2017) 1-7.
7. S. Torres-Cadenas, J. Reyes-Gasga, A. Bravo-Patiño, I. Betancourt, M.E. Contreras-García, J. Magn. Mater. 432 (2017) 410-417.
8. J.J. Went, G.W. Rathenau, E.W. Gorter, G.W. Van Oosterhout, Phys. Rev. 86 (1952) 424-425.
9. R.C. Pullar, Prog. Mater. Sci. 57 (2012) 1191-1334.
10. S.E. Rowley, Y.-Sh. Chai, Sh.-P. Shen, Y. Sun, A.T. Jones, B.E. Watts, J.F. Scott, Sci. Rep. 6 (2016) 25724-6.
11. G.-L. Tan, W. Li, J. Am. Ceram. Soc. 98 (2015) 1812-1817.
12. A.V. Trukhanov, L.V. Panina, S.V. Trukhanov, V.A. Turchenko, M. Salem, Chin. Phys. B 25 (2016) 016102-6.
13. A.V. Trukhanov, S.V. Trukhanov, V.G. Kostishin, L.V. Panina, M.M. Salem, I.S. Kazakevich, V.A. Turchenko, V.V. Kochervinskii, D.A. Krivchenya, Phys. Sol. State 59 (2017) 737-745.
14. S.V. Trukhanov, A.V. Trukhanov, V.A. Turchenko, An.V. Trukhanov, E.L. Trukhanova, D.I. Tishkevich, V.M. Ivanov, T.I. Zubar, M. Salem, V.G. Kostishyn, L.V. Panina, D.A. Vinnik, S.A. Gudkova, Ceram. Int. 44 (2018) 290-300.
15. G.-L. Tan, H.-H. Sheng, Acta Mater. 121 (2016) 144-151.
16. T. Kaur, J. Sharma, S. Kumar, A.K. Srivastava, Cryst. Res. Technol. 52 (2017) 1700098-8.
17. X. Xu, F. Huang, Y. Shao, M. Zhou, X. Ren, X. Lu, J. Zhu, Phys. Chem. Chem. Phys. 19 (2017) 18023-18029.
18. P. Kumar, A. Gaur, Appl. Phys. A 123 (2017) 732-8.
19. P. Kumar, A. Gaur, Ceram. Int. 43 (2017) 16403-16407.
20. P. Kumar, A. Gaur, R.K. Kotnal, Ceram. Int. 43 (2017) 1180-1185.
21. S. Kumar, S. Supriya, M. Kar, Mater. Res. Express 4 (2017) 126302-8.
22. S. Prathap, W. Madhuri, J. Magn. Mater. 430 (2017) 114-122.
23. V.Yu. Ivanov, A.M. Balbashov, A.A. Mukhin, L.D. Iskhakova, M.E. Voronchikhina, JETP 124 (2017) 604-611.
24. A.M. Balbashov, M.E. Voronchikhina, L.D. Iskhakova, V.Yu. Ivanov, A.A. Mukhin, Low Temp. Phys. 43 (2017) 971-976.
25. H. Izadkhan, S. Zare, S. Somu, K. Micro, F. Lombardi, C. Vittoria, MRS Comm. 7 (2017) 97-101.
26. T. Kimura, Annu. Rev. Condens. Matter Phys. 3 (2012) 93-110.
27. G. Tan, X. Chen, J. Magn. Mater. 327 (2013) 87-90.

28. V.G. Kostishyn, L.V. Panina, A.V. Timofeev, L.V. Kozhitov, A.N. Kovalev, A.K. Zyuzin, J. Magn. Mater. 400 (2016) 327-332.
29. A.S. Mikheykin, E.S. Zhukova, V.I. Torgashev, A.G. Razumnaya, Y.I. Yuzyuk, B.P. Gorshunov, A.S. Prokhorov, A.E. Sashin, A.A. Bush, M. Dressel, Eur. Phys. J. B 87 (2014) 232-9.
30. Sh.-P. Shen, Y.-Sh. Chai, J.-Z. Cong, P.-J. Sun, J. Lu, L.-Q. Yan, Sh.-G. Wang, Y. Sun, Phys. Rev. B 90 (2014) 180404R-5.
31. P. Wang, H. Xiang, Phys. Rev. X 4 (2014) 011035-6.
32. D.A. Vinnik, A.Yu. Tarasova, D.A. Zherebtsov, L.S. Mashkovtseva, S.A. Gudkova, S. Nemrava, A.K. Yakushechkina, A.S. Semisalova, L.I. Isaenko, R. Niewa, Ceram. Int. 41 (2015) 9172-9176.
33. D.A. Vinnik, A.B. Ustinov, D.A. Zherebtsov, V.V. Vitko, S.A. Gudkova, I. Zakharchuk, E. Lähderanta, R. Niewa, Ceram. Int. 41 (2015) 12728-12733.
34. A.V. Trukhanov, S.V. Trukhanov, L.V. Panina, V.G. Kostishyn, D.N. Chitanov, I.S. Kazakevich, An.V. Trukhanov, V.A. Turchenko, M.M. Salem, Ceram. Int. 43 (2017) 5635-5641.
35. A.V. Trukhanov, L.V. Panina, V.G. Kostishyn, S.H. Jabarov, V.V. Korovushkin, S.V. Trukhanov, E.L. Trukhanova, Ceram. Int. 43 (2017) 12822-12827.
36. A. Baykal, I.A. Auwal, S. Güner, H. Sözeri, J. Magn. Mater. 430 (2017) 29-35.
37. S.V. Trukhanov, A.V. Trukhanov, V.G. Kostishyn, L.V. Panina, An.V. Trukhanov, V.A. Turchenko, D.I. Tishkevich, E.L. Trukhanova, O.S. Yakovenko, L.Yu. Matzui, Dalton Trans. 46 (2017) 9010-9021.
38. S.V. Trukhanov, A.V. Trukhanov, V.G. Kostishyn, L.V. Panina, An.V. Trukhanov, V.A. Turchenko, D.I. Tishkevich, E.L. Trukhanova, V.V. Oleynik, E.S. Yakovenko, L.Yu. Matzui, D.A. Vinnik, J. Magn. Mater. 442 (2017) 300-310.
39. S.V. Trukhanov, A.V. Trukhanov, V.G. Kostishyn, L.V. Panina, An.V. Trukhanov, V.A. Turchenko, D.I. Tishkevich, E.L. Trukhanova, O.S. Yakovenko, L.Yu. Matzui, D.A. Vinnik, D.V. Karpinsky, J. Phys. Chem. Sol. 111 (2017) 142-152.
40. N. Hill, J. Phys. Chem. B 104 (2000) 6694-6709.
41. S.V. Trukhanov, A.V. Trukhanov, V.G. Kostishin, L.V. Panina, I.S. Kazakevich, V.A. Turchenko, V.V. Kochervinskiy, JETP Lett. 103 (2016) 100-105.
42. Y. Tokunaga, Y. Kaneko, D. Okuyama, S. Ishiwata, T. Arima, S. Wakimoto, K. Kakurai, Y. Taguchi, Y. Tokura, Phys. Rev. Lett. 105 (2010) 257201-4.
43. O.T. Ozkan, H. Erkalfa, J. Eur. Ceram. Soc. 14 (1994) 351-358.
44. C.-C. Huang, A.-H. Jiang, Y.-H. Hung, C.-H. Liou, Y.-C. Wang, C.-P. Lee, T.-Y. Hung, C.-C. Shaw, M.-F. Kuo, C.-H. Cheng, J. Magn. Mater. 451 (2018) 288-294.
45. J. Töpfer, S. Schwarzer, S. Senz, D. Hesse, J. Eur. Ceram. Soc. 25 (2005) 1681-1688.
46. A.V. Trukhanov, V.O. Turchenko, I.A. Bobrikov, S.V. Trukhanov, I.S. Kazakevich, A.M. Balagurov, J. Magn. Mater. 393 (2015) 253-259.
47. V.A. Turchenko, A.V. Trukhanov, I.A. Bobrikov, S.V. Trukhanov, A.M. Balagurov, J. Surf. Investig. 9 (2015) 17-23.
48. V.A. Turchenko, A.V. Trukhanov, I.A. Bobrikov, S.V. Trukhanov, A.M. Balagurov, Crystallogr. Rep. 60 (2015) 629-635.
49. S.V. Trukhanov, A.V. Trukhanov, V.O. Turchenko, V.G. Kostishin, L.V. Panina, I.S. Kazakevich, A.M. Balagurov, J. Magn. Mater. 417 (2016) 130-136.

50. S.V. Trukhanov, A.V. Trukhanov, V.A. Turchenko, V.G. Kostishyn, L.V. Panina, I.S. Kazakevich, A.M. Balagurov, *J. Alloy Compd.* 689 (2016) 383-393.
51. V.L. Aksenov, A.M. Balagurov, *Phys. Usp.* 59 (2016) 279-303.
52. H.M. Rietveld, *J. Appl. Cryst.* 2 (1969) 65-71.
53. J. Rodriguez-Carvajal, *Phys. B* 192 (1993) 55-69.
54. V.D. Doroshev, V.A. Borodin, V.I. Kamenev, A.S. Mazur, T.N. Tarasenko, A.I. Tovstolytkin, S.V. Trukhanov, *J. Appl. Phys.* 104 (2008) 093909-13.
55. S.V. Trukhanov, A.V. Trukhanov, A.N. Vasil'ev, A. Maignan, H. Szymczak, *JETP Lett.* 85 (2007) 507-512.
56. V.V. Kochervinskii, E.V. Chubunova, Yu.Yu. Lebedinskii, N.A. Shmakova, *Polymer Sci., Ser. A* 53 (2011) 929-949.
57. S.V. Trukhanov, A.V. Trukhanov, V.G. Kostishyn, L.V. Panina, V.A. Turchenko, I.S. Kazakevich, A.V. Trukhanov, E.L. Trukhanova, V.O. Natarov, A.M. Balagurov, *J. Magn. Magn. Mater.* 426 (2017) 554-562.
58. E.W. Gorter, *Proc. IRE* 43 (1955) 1945-1973.
59. A.V. Trukhanov, S.V. Trukhanov, L.V. Panina, V.G. Kostishyn, I.S. Kazakevich, A.V. Trukhanov, E.L. Trukhanova, V.O. Natarov, V.A. Turchenko, M.M. Salem, A.M. Balagurov, *J. Magn. Magn. Mater.* 426 (2017) 487-496.
60. V.V. Atuchin, D.A. Vinnik, T.A. Gavrilova, S.A. Gudkova, L.I. Isaenko, X. Jiang, L.D. Pokrovsky, I.P. Prosvirin, L.S. Mashkovtseva, Z. Lin, *J. Phys. Chem. C* 120 (2016) 5114-5123.
61. R.D. Shannon, *Acta Crystallogr. A* 32 (1976) 751-767.
62. T. Chatterji, T.C. Hansen, M. Brunelli, P.F. Henry, *Appl. Phys. Lett.* 94 (2009) 241902-3.
63. S.M. El-Sayed, T.M. Meaz, M.A. Amer, H.A. El Shersaby, *Physica B* 426 (2013) 137-143.
64. V.G. Kostishyn, L.V. Panina, L.V. Kozhitov, A.V. Timofeev, A.N. Kovalev, *J. Alloy Compd.* 645 (2015) 297-300.
65. M.A. Gilleo, *Phys. Rev.* 109 (1958) 777-781.
66. S.V. Trukhanov, A.V. Trukhanov, S.G. Stepin, H. Szymczak, C.E. Botez, *Phys. Sol. State* 50 (2008) 886-893.
67. J.-M. Le Breton, J. Teillet, G. Wiesinger, A. Morel, F. Kools, P. Tenaud, *IEEE Trans. Magn.* 38 (2002) 2952-2954.
68. S.V. Trukhanov, A.V. Trukhanov, A.N. Vasiliev, A.M. Balagurov, H. Szymczak, *JETP* 113 (2011) 819-825.
69. P.G. Radaelli, G. Iannone, M. Marezio, H.Y. Hwang, S.-W. Cheong, J.D. Jorgensen, D.N. Argyriou, *Phys. Rev. B* 56 (1997) 8265-8276.
70. S.V. Trukhanov, A.V. Trukhanov, H. Szymczak, C. E. Botez, A. Adair, *J. Low Temp. Phys.* 149 (2007) 185-199.
71. S.V. Trukhanov, A.V. Trukhanov, A.N. Vasiliev, H. Szymczak, *JETP* 111 (2010) 209-214.
72. P. Novak, J. Rusz, *Phys. Rev. B* 71 (2005) 184433-6.
73. M. Okube, J. Yoshizaki, T. Toyoda, S. Sasaki, *J. Appl. Cryst.* 49 (2016) 1433-1442.
74. J.B. Goodenough, *J. Phys. Chem. Solids* 6 (1958) 287-297.

FIGURE CAPTIONS

Fig. 1. Rietveld refined NPD spectrum for the $\text{BaFe}_{10.8}\text{In}_{1.2}\text{O}_{19}$ at 300 K (a) and 730 K (b) obtained in frame of $P6_3/mmc$ (No 194) space group. It is shown the experimental points (crosses), calculated function (upper curve), difference curve (lower curve) normalized to the statistical error and diffraction peak positions (vertical bars) for the atomic (upper row) and magnetic (lower row) structure.

Fig. 2. Schematic representation of the certain oxygen surrounding of each iron crystallographic position.

Fig. 3. Powder neutron diffraction spectrum for $\text{BaFe}_{11.9}\text{In}_{0.1}\text{O}_{19}$ sample, obtained at 300 K room temperature and processed by the Rietveld method in frame of $P6_3/mc$ (No 186) space group. The experimental points (crosses), the calculated function (upper curve) and the difference curve (lower curve) normalized to the statistical error are shown. Top and bottom vertical bars are the calculated positions of the diffraction peaks of the atomic and magnetic structure, respectively.

Fig. 4. Temperature dependence of the a (a) and c (b) parameters and V (c) volume of unit cell for the $\text{BaFe}_{11.9}\text{In}_{0.1}\text{O}_{19}$ (full symbols) and $\text{BaFe}_{10.8}\text{In}_{1.2}\text{O}_{19}$ (open symbols).

Fig. 5. Temperature dependence of the main Fe-O bond lengths for the $\text{BaFe}_{11.9}\text{In}_{0.1}\text{O}_{19}$ (left column) and $\text{BaFe}_{10.8}\text{In}_{1.2}\text{O}_{19}$ (right column): (a) – Fe3-O2, Fe2-O1 and Fe4-O3; (b) – Fe5-O2, Fe1-O4 and Fe4-O5; (c) – Fe5-O1, Fe3-O4 and Fe2-O3. Dash line is liner fitting.

Fig. 6. Temperature dependence of the main Fe-O-Fe bond angles for the $\text{BaFe}_{11.9}\text{In}_{0.1}\text{O}_{19}$ (left column) and $\text{BaFe}_{10.8}\text{In}_{1.2}\text{O}_{19}$ (right column): (a) – Fe3-O4-Fe5 and Fe2-O3-Fe4; (b) – Fe5-O2-Fe5 and Fe5-O1-Fe5; (c) – Fe4-O3-Fe4 and Fe5-O4-Fe5. Dash line is liner fitting.

Fig. 7. Field dependence of the dielectric polarization at room temperature (300 K) for the $\text{BaFe}_{12-x}\text{In}_x\text{O}_{19}$ hexaferrites with $x = 0.1$ (a) and 1.2 (b).

Fig. 8. Scheme of distortions of oxygen octahedra around iron cations in Fe4 and Fe44-2b (a, b) and Fe5 and Fe55 - 6c (c, d) positions in frame of $P6_3/mc$ (No 186) space group caused by a decrease in the symmetry of a unit cell from $P6_3/mmc$ (No 194) space group.

Fig. 9. Temperature dependence of the specific magnetization (a) in 1 T and the inverse value of the magnetic susceptibility (b) for the $\text{BaFe}_{11.9}\text{In}_{0.1}\text{O}_{19}$ and $\text{BaFe}_{10.8}\text{In}_{1.2}\text{O}_{19}$ in heating (full circle) and cooling (open circle) modes. Insert demonstrates the the temperature derivative of the specific magnetization with T_c indicating.

Fig. 10. Comparative temperature dependence of the magnetic moment per iron ion for the $\text{BaFe}_{11.9}\text{In}_{0.1}\text{O}_{19}$ (full circle) and $\text{BaFe}_{10.8}\text{In}_{1.2}\text{O}_{19}$ (open circle) samples in different positions: (a) - 2a, (b) - 2b, (c) – $4f_{IV}$, (d) - $4f_{VI}$, (e) - 12k, (f) - the total magnetic moment per iron ion obtained by NPD. Dash line is polinomial fitting.

Fig. 11. Illustration of the polarization origin mechanism in the $\text{BaFe}_{12-x}\text{In}_x\text{O}_{19}$ samples as a consequence of the distortion of the oxygen octahedrons. (a) - normal oxygen octahedron with a small Fe^{3+} cation at the central position, (b) – noncentrosymmetric polar distortion of the Fe-O bond lengths as a result of the displacement of the Fe^{3+} cation to one of the O^{2-} anions.

Table 1. The crystal structure parameters, atomic coordinates and reliability R-factors for the BaFe_{10.8}In_{1.2}O₁₉ solid solution obtained from NPD data (SG = P6₃/mmc (№194)) at different temperatures by the Rietveld method. Atoms are in positions : Ba (2d) (2/3, 1/3, 1/4), (Fe/In)1 (2a) (0, 0, 0); (Fe/In)2 (2b) (0, 0, 1/4); (Fe/In)3 (4f_{IV}*) (1/3, 2/3, z); (Fe/In)4 (4f_{VI}*) (1/3, 2/3, z); (Fe/In)5 (12k) (x, 2x, z); O1 (4e) (0, 0, z); O2 (4f) (1/3, 2/3, z); O3 (6h) (x, 2x, 1/4); O4 (12k) (x, 2x, z); O5 (12k) (x, 2x, z). f_{IV} - tetrahedral oxygen coordination; f_{VI} - octahedral oxygen coordination.

Atomic parameters	Temperature				
	10 K	100 K	150 K	300 K	730 K
<i>a</i> , (Å)	5.9337(6)	5.9335(4)	5.9332(3)	5.9326(2)	5.9643(2)
<i>c</i> , (Å)	23.4477(2)	23.4452(3)	23.4456(3)	23.4458(9)	23.5980(9)
<i>V</i> , (Å ³)	714.97(11)	714.82(2)	714.86(4)	714.64(5)	726.98(5)
Fe3/In3 (4f_{IV})					
<i>z</i>	0.0304(8)	0.0258(3)	0.0254(3)	0.0246(3)	0.0253(3)
Fe4/In4 (4f_{VI})					
<i>z</i>	0.1895(7)	0.1891(5)	0.1893(5)	0.1821(3)	0.1873(3)
Fe5/In5 (12k)					
<i>x</i>	0.1592(18)	0.1598(2)	0.1632(2)	0.1664(9)	0.1672(7)
<i>z</i>	-0.1074(3)	-0.1072(3)	-0.1071(3)	-0.1071(1)	-0.1074(1)
<i>B_{iso}</i>	0.103(5)	0.205(3)	0.478(3)	0.345(4)	0.912(5)
O1 (4e)					
<i>z</i>	0.1389(9)	0.1386(2)	0.1435(4)	0.1458(4)	0.1475(4)
O2 (4f)					
<i>z</i>	-0.0452(9)	-0.0462(7)	-0.0482(9)	-0.0517(4)	-0.0559(4)
O3 (6h)					
<i>x</i>	0.1622(4)	0.1642(2)	0.1672(4)	0.1784(19)	0.1798(18)
O4 (12k)					
<i>x</i>	0.1493(2)	0.1503(3)	0.1523(2)	0.1579(14)	0.1547(12)
<i>z</i>	0.0541(5)	0.0544(5)	0.0542(5)	0.0531(2)	0.0513(2)
O5 (12k)					
<i>x</i>	0.5084(2)	0.5081(3)	0.5082(4)	0.5084(2)	0.5027(2)
<i>z</i>	0.1506(4)	0.1508(5)	0.1507(3)	0.1506(2)	0.1478(2)
<i>B_{iso}</i>	0.301(3)	0.351(3)	0.450(3)	0.457(3)	0.871(3)
<i>R_{wp}</i> , %	9.17	5.32	3.42	3.82	4.92
<i>R_{exp}</i> , %	6.57	4.63	5.32	2.71	3.87
<i>R_B</i> , %	11.2	9.36	7.64	6.40	7.01
<i>R_{Mag}</i> , %	12.3	5.43	6.34	5.94	--
<i>χ</i> ²	1.95	1.87	2.03	1.98	1.61

Table 2. The crystal structure parameters, atomic coordinates and reliability R-factors for the BaFe_{11.9}In_{0.1}O₁₉ and BaFe_{10.8}In_{1.2}O₁₉ solid solutions obtained from NPD data (SG = P6₃mc (№186)) at 300 K room temperature by the Rietveld method. Atoms are in positions : Ba (2b) (2/3, 1/3, z); (Fe/In)1 (2a) (0, 0, z); (Fe/In)2 (2a) (0, 0, z); (Fe)3 (2b) (1/3, 2/3, z); (Fe)33 (2b) (1/3, 2/3, z); (Fe)4 (2b) (1/3, 2/3, z); (Fe)44 (2b) (1/3, 2/3, z); (Fe/In)5 (6c) (x, 2x, z); (Fe/In)55 (6c) (x, 2x, z); O1 (2a) (0, 0, z); O11 (2a) (0, 0, z); O2 (2b) (1/3, 2/3, z); O22 (2b) (1/3, 2/3, z); O3 (6c) (x, 2x, z); O4 (6c) (x, 2x, z); O44 (6c) (x, 2x, z); O5 (6c) (x, 2x, z); O55 (6c) (x, 2x, z).

Atomic parameters	Substitution level x	
	0.1	1.2
<i>a</i> , (Å)	5.8954(1)	5.9327(2)
<i>c</i> , (Å)	23.2168(5)	23.4456(9)
<i>V</i> , (Å ³)	698.80(2)	714.65(5)
Ba (2b) ,		
<i>z</i>	0.2588(15)	0.2443(21)
Fe1 (2a)		
<i>z</i>	-0.0037(0)	-0.0082(12)
Fe2 (2a)		
<i>z</i>	0.2415(7)	0.2551(9)
Fe3 (2b)		
<i>z</i>	0.0337(8)	0.0248(10)
Fe33 (2b)		
<i>z</i>	0.4789(8)	0.4734(9)
Fe4 (2b)		
<i>z</i>	0.1822(9)	0.1745(9)
Fe44(2b)		
<i>z</i>	0.3035(8)	0.2979(9)
Fe5 (6c)		
<i>x</i>	0.1644(14)	0.1660(0)
<i>z</i>	-0.1062(9)	-0.1167(9)
Fe55 (6c)		
<i>x</i>	0.1680(0)	0.1691(18)
<i>z</i>	0.6112(9)	0.5975(9)
O1 (2a)		
<i>z</i>	0.1599(14)	0.1357(12)
O11 (2a)		
<i>z</i>	0.3574(13)	0.3441(13)
O2 (2b)		
<i>z</i>	0.9399(12)	0.9361(15)
O22 (2b)		
<i>z</i>	0.5483(13)	0.5417(15)
O3 (6c)		
<i>x</i>	0.1828(16)	0.1819(21)
<i>z</i>	0.2509(14)	0.2485(11)

O4 (6c)			
	<i>x</i>	0.1519(22)	0.1619
	<i>z</i>	0.0494(10)	0.0416(10)
O44 (6c)			
	<i>x</i>	0.1589(0)	0.1514(22)
	<i>z</i>	0.4463(13)	0.4369(10)
O5 (6c)			
	<i>x</i>	0.5059(0)	0.4987(26)
	<i>z</i>	0.1541(11)	0.1415(0)
O55 (6c)			
	<i>x</i>	0.5006(0)	0.5055(0)
	<i>z</i>	0.3545(12)	0.3429(4)
	R_{wp} , %	13.5	16.5
	R_{exp} , %	10.04	11.92
	R_B , %	7.13	6.96
	R_{Mag} , %	7.47	9.45
	χ^2	1.81	1.85

Table 3. The iron cation-ligand distances in the crystal structure of $\text{BaFe}_{12-x}\text{In}_x\text{O}_{19}$ solid solutions with $x = 0.1$ and 1.2 determined at 300 K room temperature by the Rietveld method in framework of $P6_3/mmc$ (No. 194) space group.

Cations		Oxygen surroundings	Substitution level, x	
			0.1	1.2
		Distances, Å		
Fe1 (2a)	O4	6x	2.0148	2.0399
	O3		1.8210	1.8221
Fe2 (2b)	O1	2x	2.3011	2.4357
	O2		1x	1.8959
Fe3 (4f _{IV})	O4	1x	1.8795	1.9254
	O4	2x	1.8799	1.9259
	O5	2x	1.9654	1.9654
Fe4 (4f _{VI})	O5	1x	1.9658	1.9658
	O3	1x	2.1484	2.1484
	O3	2x	2.1488	2.1488
	O1	1x	1.9708	1.9619
Fe5 (12k)	O5	1x	1.9279	1.9261
	O5	1x	1.9288	1.9261
	O4	1x	2.1041	2.1317
		1x	2.1051	2.1317
		1x	2.1359	2.1288
	O2	1x		

Table 4. The iron cation-ligand distances and dipole electric moments of oxygen polyhedra in the crystal structure of $\text{BaFe}_{12-x}\text{In}_x\text{O}_{19}$ solid solutions with $x = 0.1$ and 1.2 determined at 300 K room temperature by the Rietveld method in framework of $\text{P6}_3/\text{mc}$ (No. 186) space group.

Cations		Oxygen surroundings	Substitution level, x	
			0.1	1.2
		Distances, Å		
Fe1 (2a)	O4	3x	1.9810	2.0327
	O44	3x	1.9954	2.0203
μ, D			0.12	0.103
Fe2 (2a)	O3	3x	1.8802	1.8754
	O11	1x	2.6906	2.0876
	O1	1x	1.8959	2.8001
μ, D			3.815	3.42
Fe3 (2b)	O4	1x	1.8876	1.8045
	O4	2x	1.8881	1.8050
	O2	1x	2.1782	2.0792
μ, D			5.28	4.339
Fe33 (2b)	O22	1x	1.6087	1.6006
	O44	1x	1.9356	2.0565
	O44	2x	1.9361	2.0569
μ, D			3.205	4.652
Fe4 (2b)	O5	2x	1.8785	1.8672
	O5	1x	1.8790	1.8677
	O3	1x	2.2153	2.3312
	O3	2x	2.2157	2.3316
μ, D			2.801	3.858
Fe44 (2b)	O3	1x	1.9607	1.9407
	O3	2x	1.9611	1.9411
	O55	2x	2.0792	2.0585
	O55	1x	2.0796	2.0589
μ, D			0.984	0.978
Fe5 (6c)	O11	1x	1.8789	1.9374
	O55	1x	1.9386	1.9364
	O55	1x	1.9390	1.9364
	O2	1x	2.0306	2.1190
	O44	1x	2.0513	2.0620
	O44	1x	2.0515	2.0620
μ, D			1.056	1.219
Fe55 (6c)	O1	1x	2.0541	1.9534
	O5	1x	1.9407	1.9938
	O5	1x	1.9407	1.9941
	O4	1x	2.1795	2.1479
	O4	1x	2.1795	2.1484
	O22	1x	2.2329	2.1365
μ, D			1.834	1.366

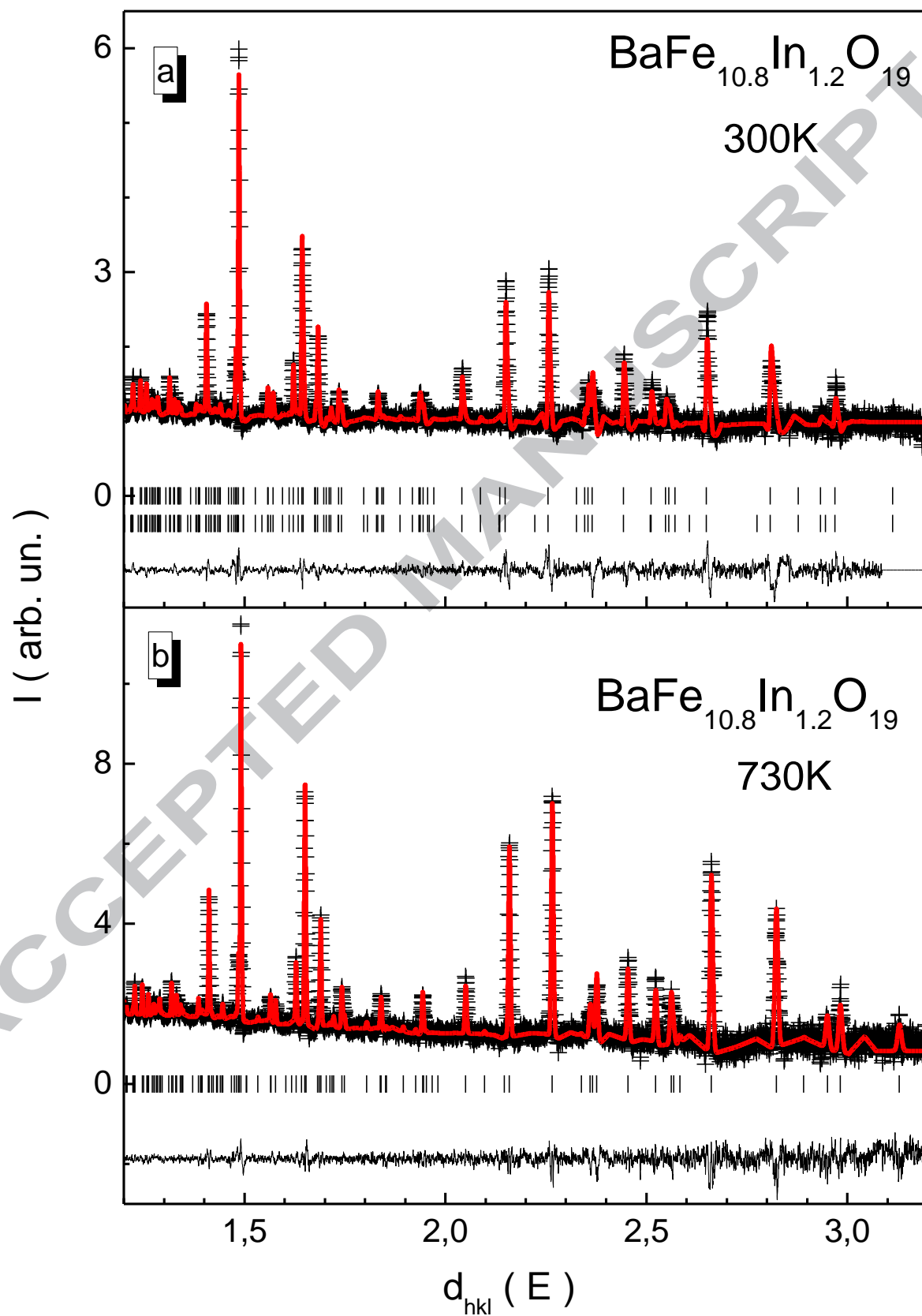


Fig. 1

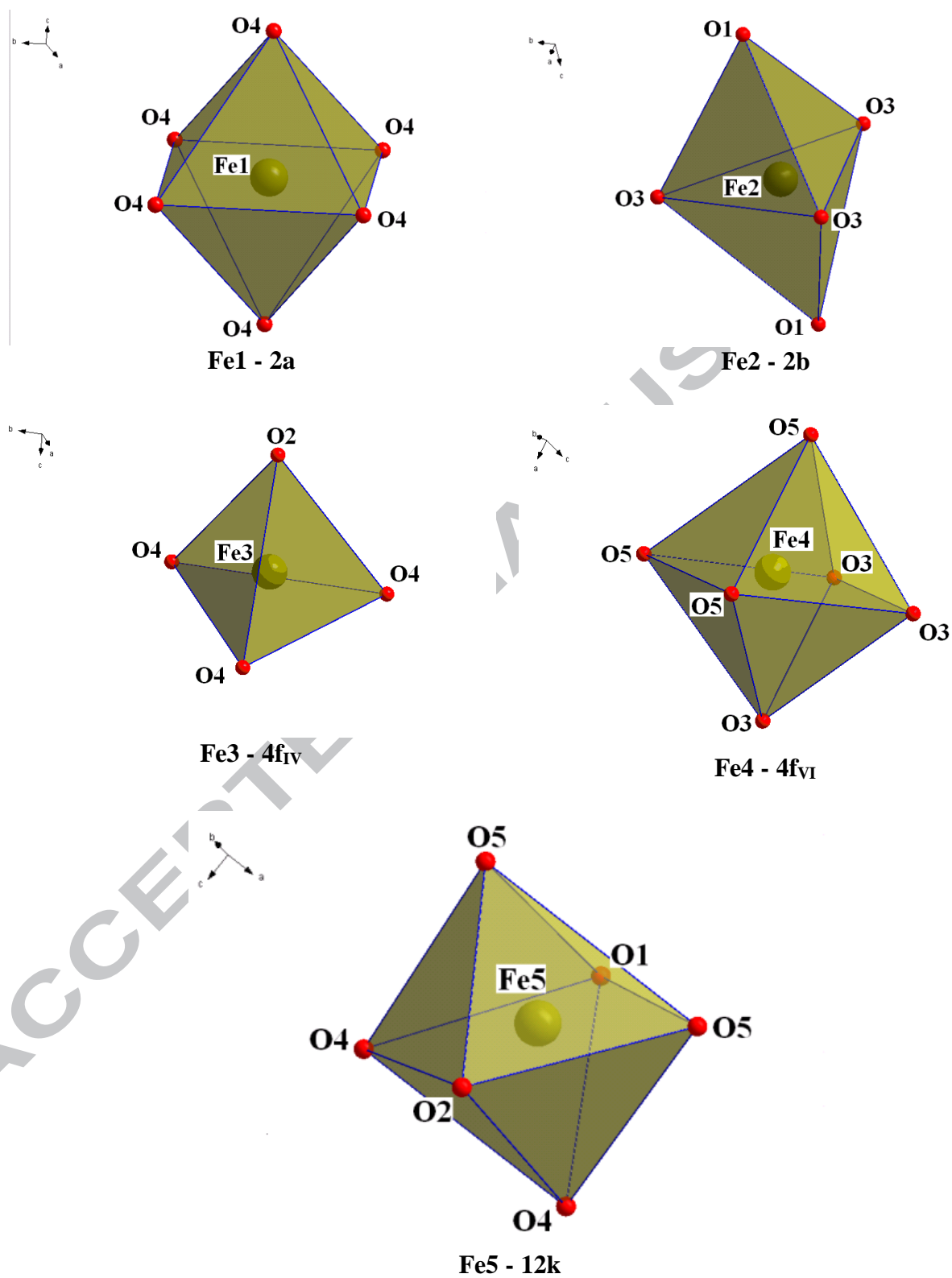


Fig. 2

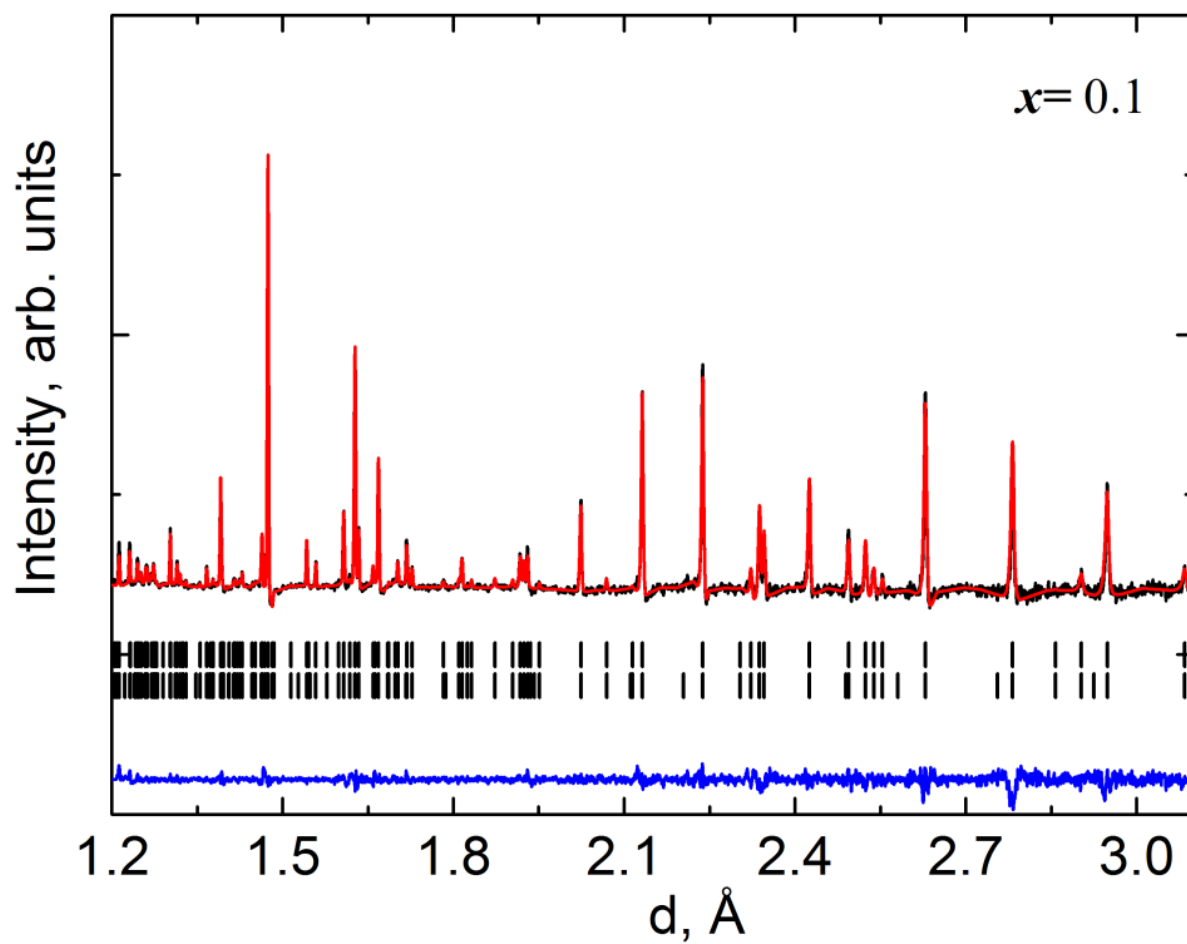


Fig. 3

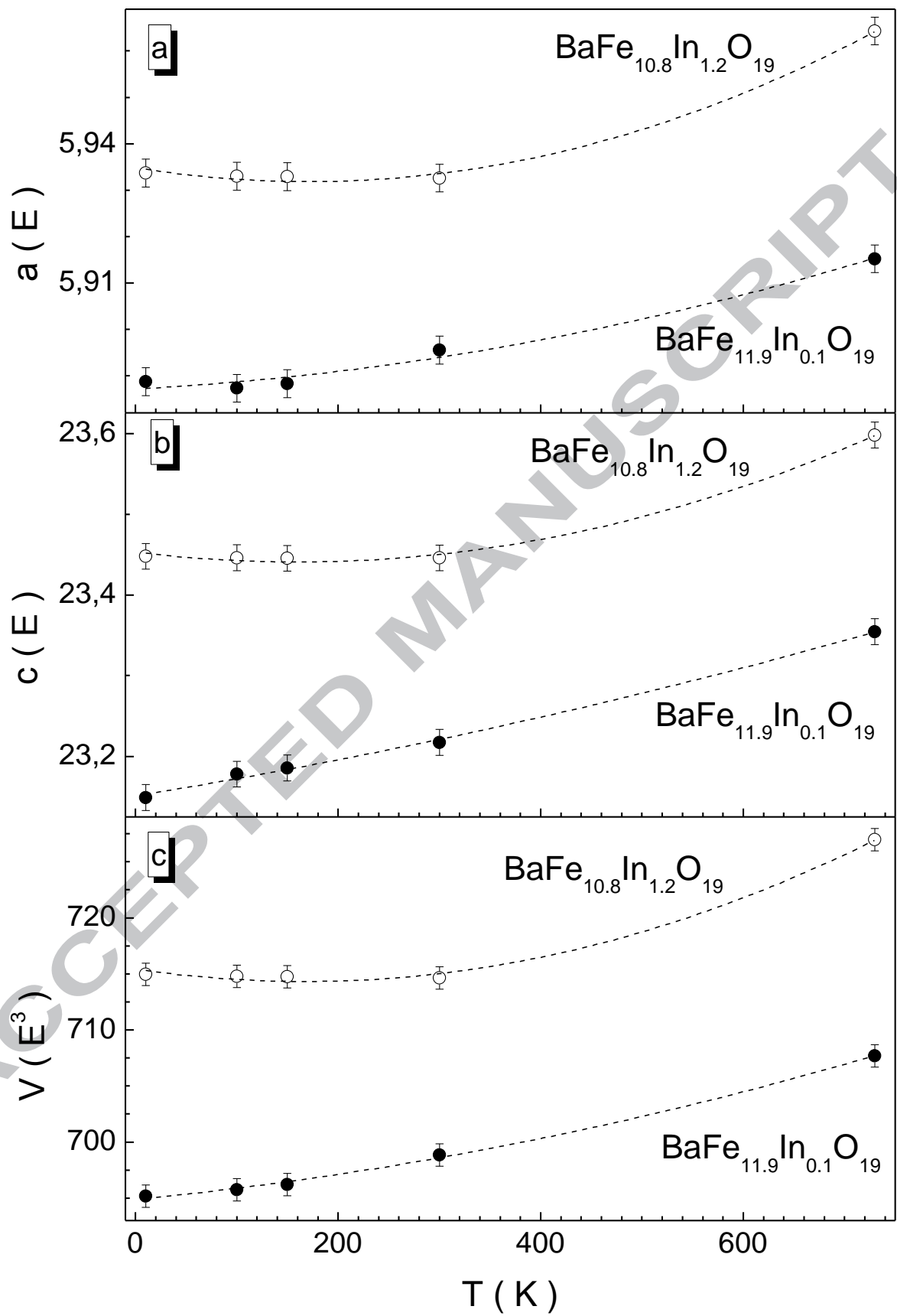


Fig. 4

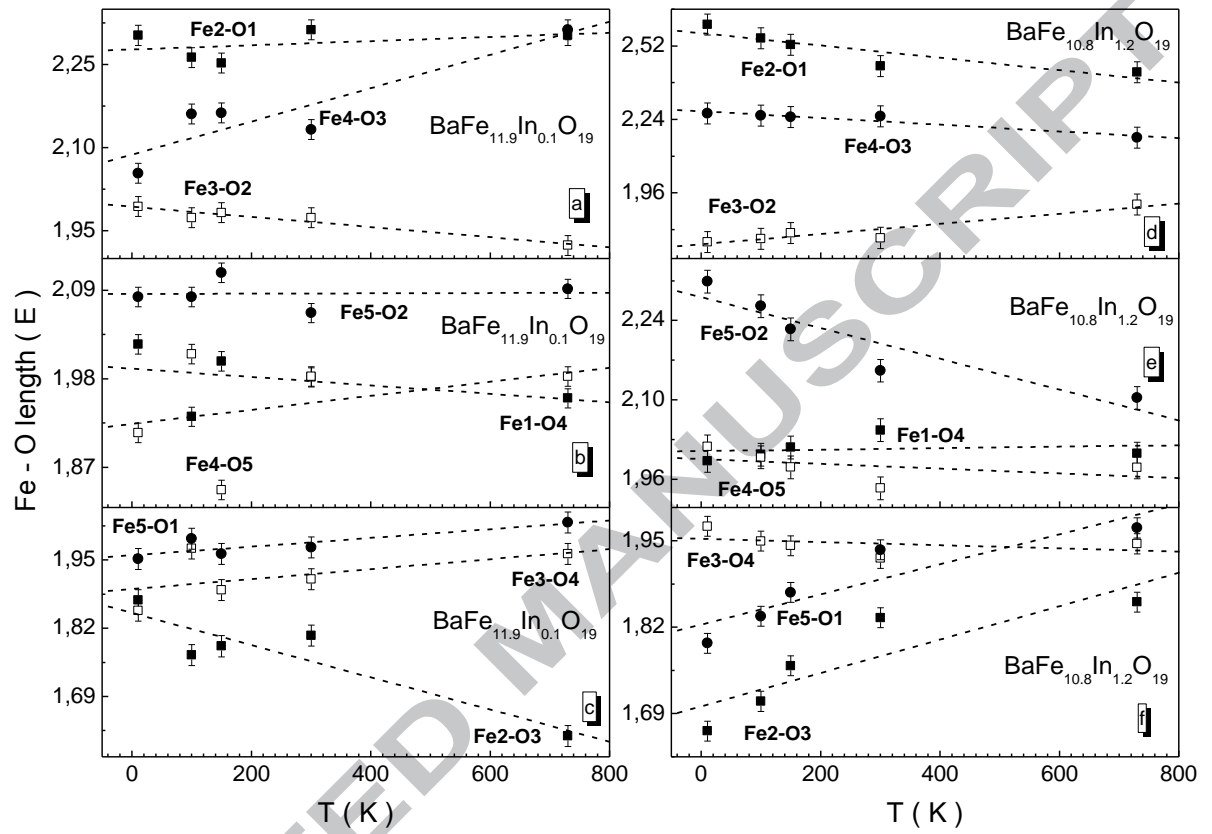


Fig. 5

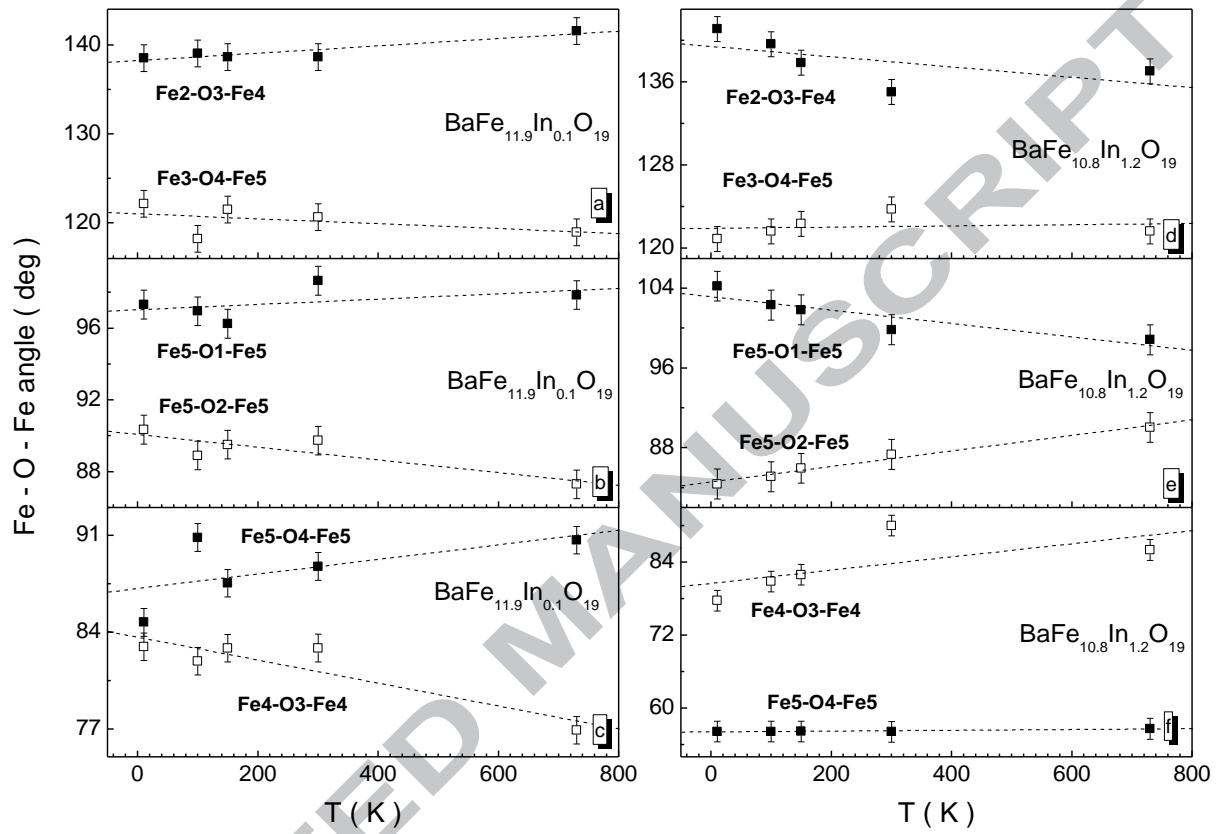


Fig. 6

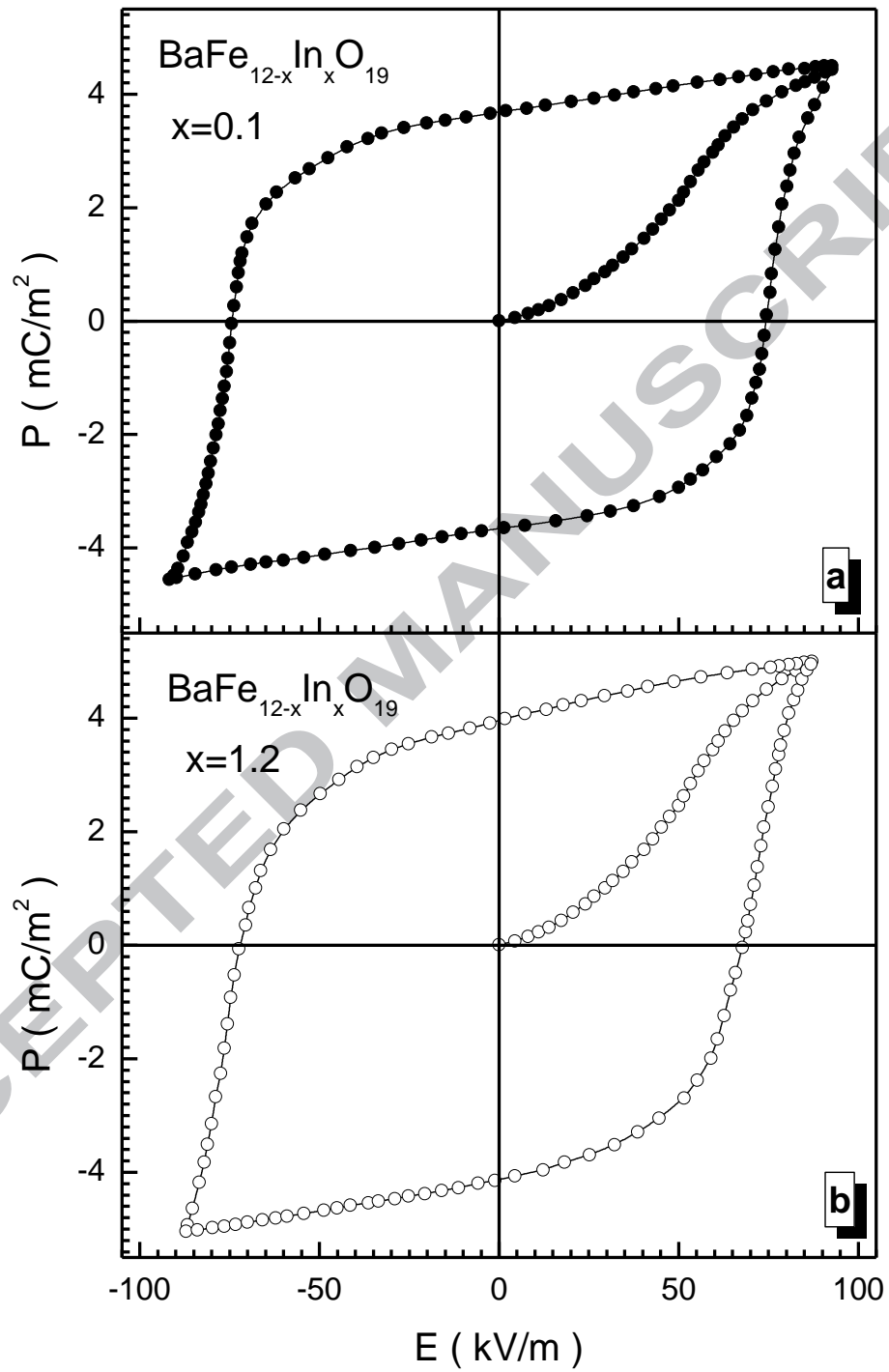


Fig. 7

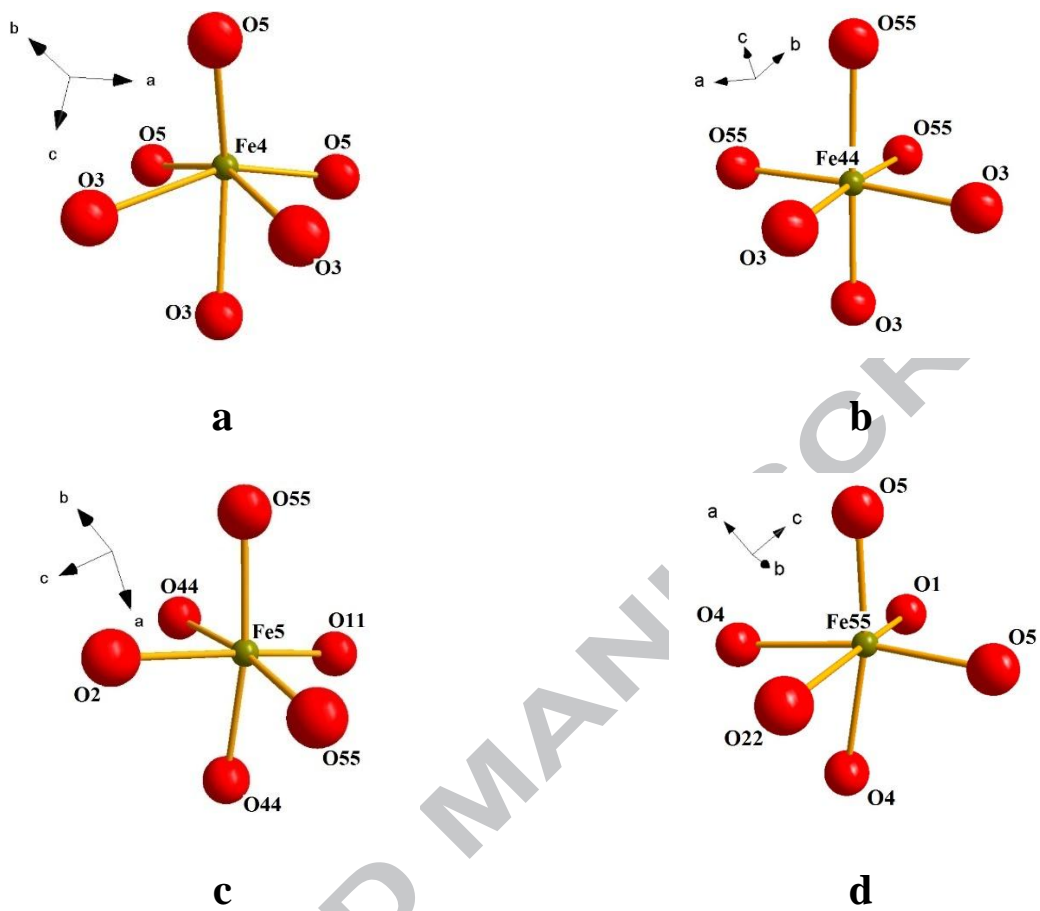


Fig. 8

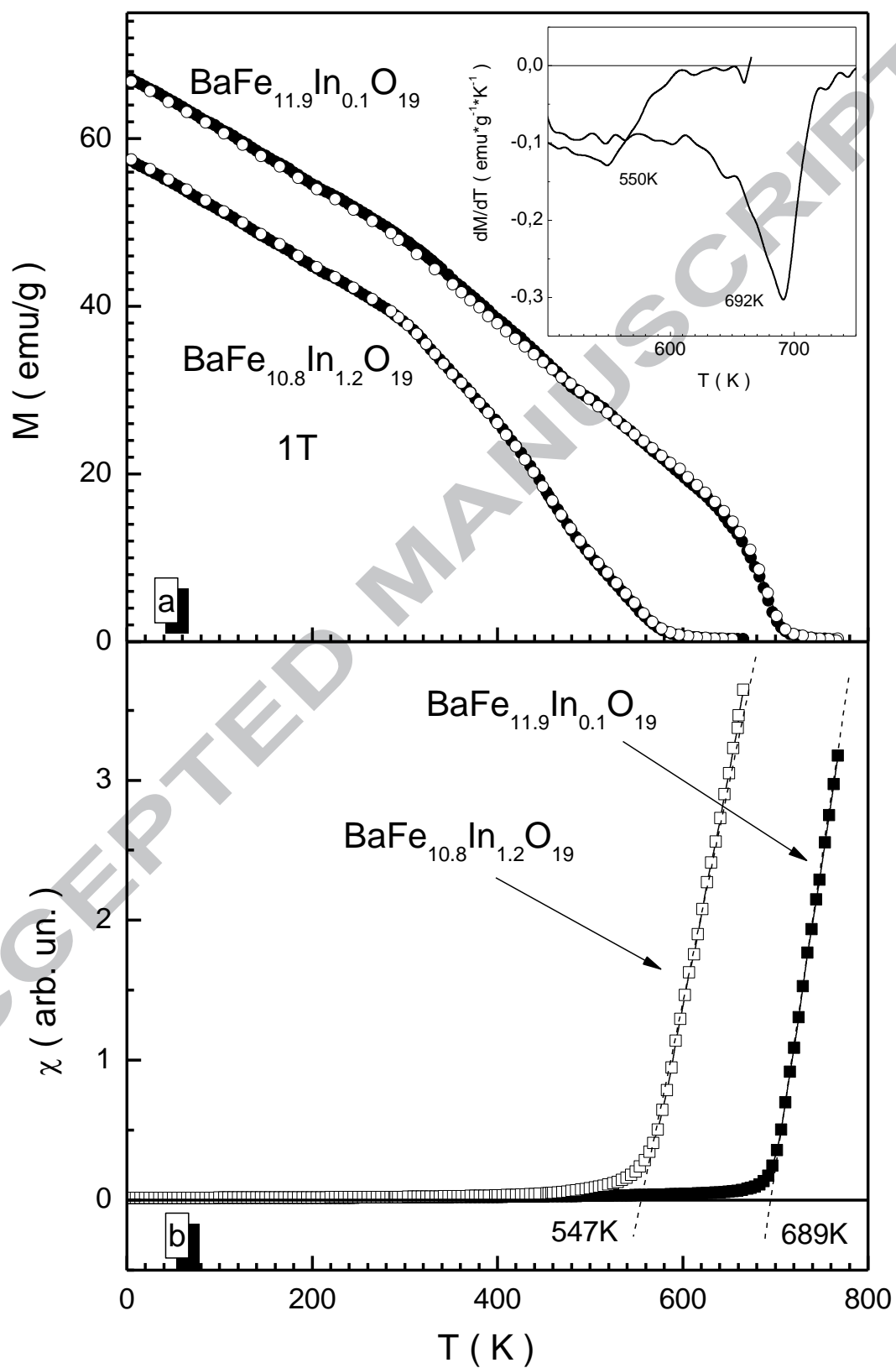


Fig. 9

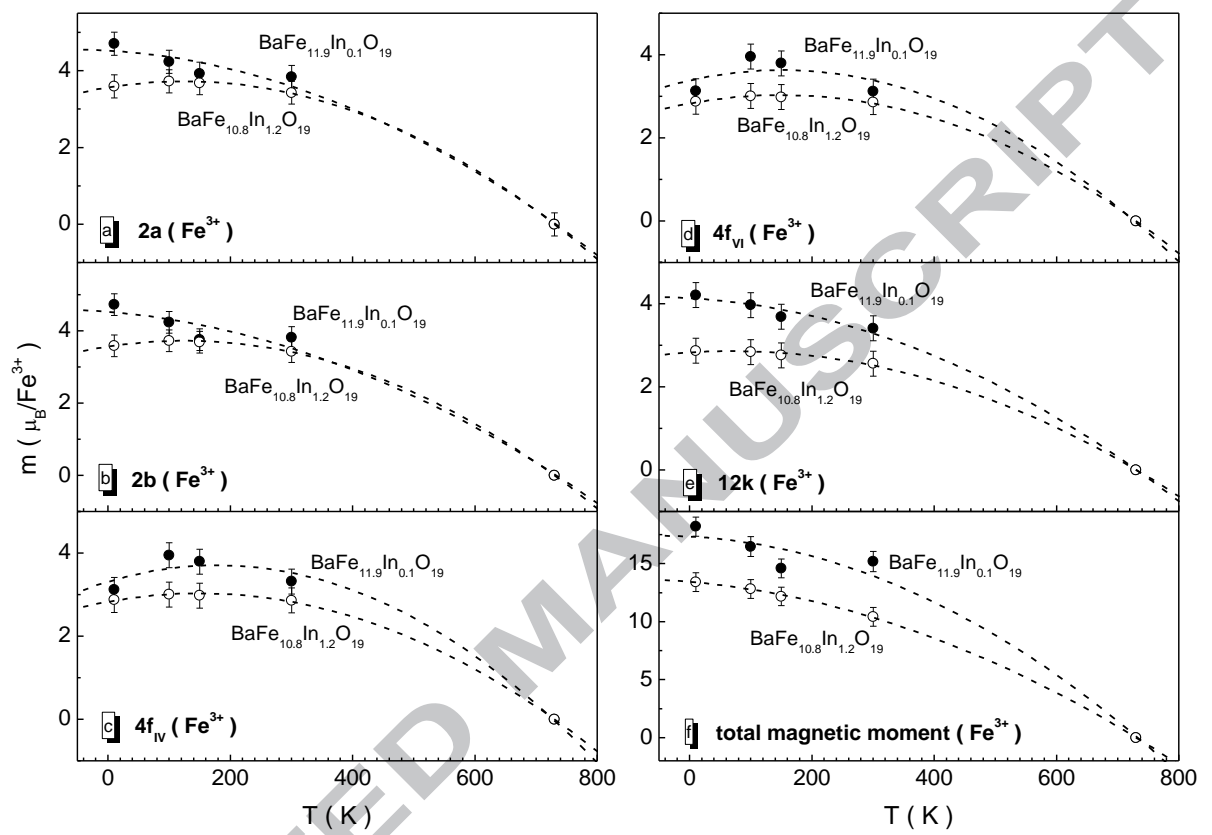


Fig. 10

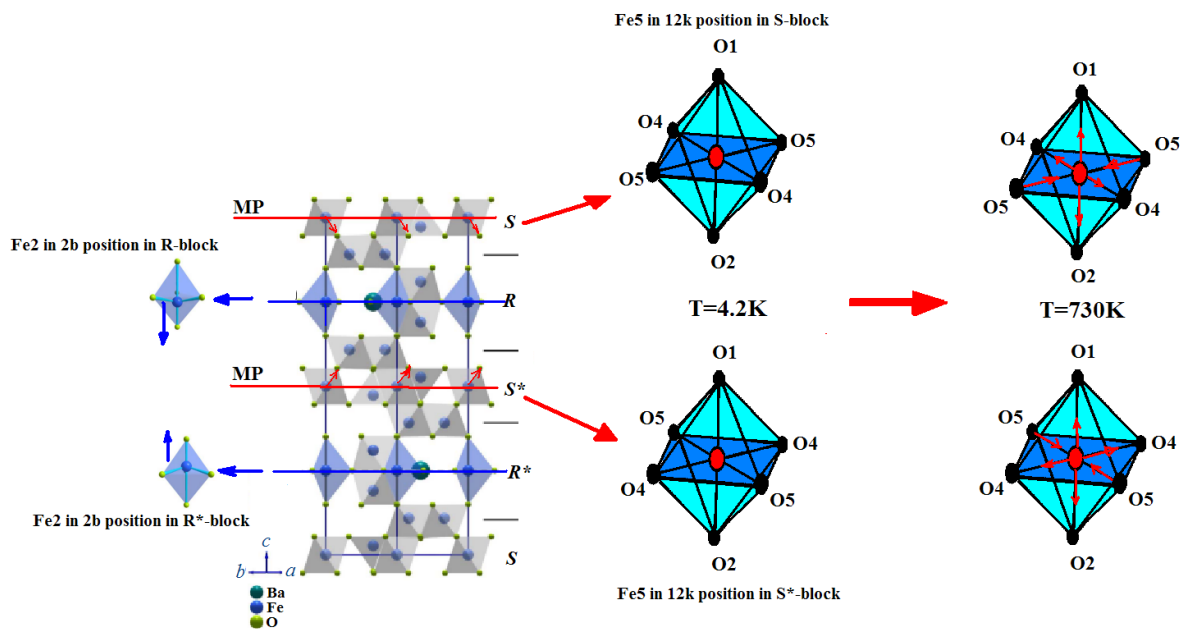


Fig. 11

Structure vs. temperature for $\text{BaFe}_{12-x}\text{In}_x\text{O}_{19}$ $x = 0.1, 1.2$ was investigated.

Atomic coordinates and lattice parameters were Rietveld refined.

Exchange interactions vs. structure were investigated.

Magnetic and dipole moments at different position per iron ion were defined.

Spontaneous polarization for these compositions was established at 300 K.

ACCEPTED MANUSCRIPT